Swinging Motion of a Kite with Suspended Control Unit Flying Turning Manoeuvres

Mark Schelbergen[1] and Roland Schmehl[1]

[1]Faculty of Aerospace Engineering, Delft University of Technology, 2629 HS Delft, Netherlands

Correspondence: Mark Schelbergen (m.schelbergen@tudelft.nl)

Abstract. The flexible membrane kite employed by some airborne wind energy systems uses a suspended control unit, which experiences a characteristic swinging motion relative to the top of the kite during sharp turning manoeuvres. This paper assesses the accuracy of a two-point kite model in resolving this swinging motion using two different approaches: approximating the motion as a transition through steady-rotation states and solving the motion dynamically. The kite model extends a discretised tether model with two rigidly linked point masses representing the control unit and wing. The tether-kite motion is solved by prescribing the trajectory of the wing point mass to replicate a figure-of-eight manoeuvre from the flight data of an existing prototype. The computed pitch and roll of the kite are compared against the attitude measurements of two sensors mounted to the wing. The two approaches compute similar pitch and roll angles during the straight sections of the figure-of-eight manoeuvre and match measurements within three degrees. However, during the turns, the dynamically solved pitch and roll angles show systematic differences compared to the steady-rotation solution. As a two-point kite model resolves the roll, the lift force may tilt along with the kite to drive turns. This important aspect of the turning mechanism cannot be modelled with single-point kite models. Moreover, the two-point kite model complements the aerodynamic model as it allows computing the angle of attack of the wing by resolving the pitch. These characteristics improve the generalisation of the kite model with little additional computational effort.

1 Introduction

Pumping airborne wind energy (AWE) systems with flexible membrane kites are reaching a technology readiness level suitable for first commercial applications. Two prominent examples are the leading developers SkySails Power GmbH using ram-air kites and Kitepower B.V. using leading-edge inflatable (LEI) kites (Vermillion et al., 2021; Fagiano et al., 2022). Both systems employ a single tether and a suspended kite control unit (KCU) for actuating the wing, as illustrated in Fig. 1. At the present stage of development, AWE systems are not optimised yet in terms of power production. Instead, the priority is improving operational reliability and demonstrating long-term operation, as well as learning how the systems perform in different wind environments (Salma et al., 2019). This knowledge will be crucial for designing the next generation of systems with increased power output.

Performance models estimate the energy generation of a specific system in a varying wind environment over extended periods of time. The most simple and computationally efficient models extend Loyd's analytic theory of tethered flight (Loyd,

Figure 1. AWE system with a 60 m^2 kite and ground station integrated in a standard 20 ft container in operation on the Caribbean island Aruba in October 2021 (photo courtesy of Kitepower B.V.).

1980) using one or more steady flight states and do not attempt modelling the turning behaviour. In a next level of model refinement, quasi-steady models prescribe a parameterised flight path to increase the resolution of the flight path. Thereby, they account for the effect of turning but do not necessarily describe the turning mechanism of the kite. Alternatively, dynamic models require incorporating a turning mechanism and can be applied in an optimal control problem (OCP) to find an optimal

30 realistic flight path. The simpler models represent the kite as a single point mass or rigid body and assume a straight tether with its mass and drag lumped to the kite. More refined models also resolve tether sag induced by lateral forces on the tether, such as gravity, centrifugal force, and aerodynamic drag. This can be conveniently done by discretising the tether. Typically, the tether is represented with lumped masses connected with rigid links or spring-damper elements (Gohl and Luchsinger, 2013; Fechner et al., 2015; Rapp et al., 2019; Williams et al., 2007; Zanon et al., 2013). Alternatively, Sánchez-Arriaga et al.

35 (2019) apply a multi-body approach using rigid rods. Fechner et al. (2015) expand the discretisation approach to the kite. The kite is represented with five point masses; four point masses represent the wing, and one additional point mass represents the suspended KCU. A lumped-mass model with spring-damper elements yields a stiff system of differential equations. Solving this system requires a small time step and is prone to numerical instabilities. These models are considered too computationally costly for performance calculation but are used for control system design.

40   To efficiently account for tether elasticity, Williams (2017) solves the 'quasi-static' tether deformation as a subroutine to solving the motion of the kite. Consequently, the loaded tether shape due to gravity, centrifugal force and aerodynamic drag is considered, while the transient motion and longitudinal vibration are neglected. The discretised tether model assumes that the entire airborne system, including tether and kite, jointly rotates around the tether attachment point at the ground. This assumed kinematic relationship works well for near-straight flights but is not representative during turning manoeuvres.

45   The choice of the kite model determines the level of abstraction required to introduce steering forces as demonstrated in the work of Fechner et al. (2015). The work presents both a single-point and a five-point kite model of a LEI kite. By resolving the roll of the kite with respect to the upper tether segment, the five-point kite model allows for a realistic incorporation of the centripetal force acting on the relatively heavy control unit. Together with the kite, the lift force of the top wing surface may tilt into turns and pull the control unit along the same turn. Additionally, the lift forces of the wing tips contribute to the
50   centripetal force. The lift coefficient of each wing surface depends on the local angle of attack and has a maximum of 1.1. The single-point model requires intricate centripetal force modelling because it lacks information about the attitude of the kite. To enable steering, it employs an artificial lateral force proportional to the steering input. The lift force of the top wing surface is assumed unaffected by this steering input and is approximately aligned with the upper tether segment. Due to this alignment, the lift force cannot exert a centripetal force on the control unit. This may explain why the lateral force coefficient of 2.59 is
55   significantly higher than the lift force coefficient of the wing tip in the five-point kite model.

In reality, the deformation of the wing due to steering input is not as simple as suggested by the latter aerodynamic models. The LEI kite of Kitepower B.V. is steered by pulling the rear bridle lines attached to one side of the wing while loosening the lines on the other side. This asymmetric actuation of the bridle line system makes the wing deform and initiate a turn. Video footage of experiments shed some light on the aero-structural deformation due to steering (Schmehl and Oehler, 2018).
60   Previous research on the topic has focused mainly on the interaction between the flow and the deforming bridled membrane wing (Breukels et al., 2013; Bosch et al., 2013; Geschiere, 2014; Duport, 2018; Oehler et al., 2018; Thedens, 2022; Folkersma, 2022; Poland, 2022; Cayon, 2022). The experimental data also indicates a pronounced dynamic interaction between the wing, the suspended KCU, and the tether during the turning manoeuvre. How much the swinging motion of the KCU relative to the wing affects the turning behaviour and the power generation of the kite has only recently been studied by Roullier (2020). An
65   improved understanding of this effect would allow for enhancing performance models of flexible membrane kites, designing more precise control algorithms, and ultimately improving the system performance.

The goal of this paper is twofold: to study the dynamics that induce the observed characteristic pitch and roll swinging motion of the kite during sharp turning manoeuvres and discuss the implications to performance modelling. Pertaining to the first goal, this paper introduces a two-point kite model that is used together with a straight and discretised tether. Firstly, the
70   motion is approximated as a transition through steady-rotation states with both tether representations. Subsequently, the motion is resolved dynamically with the discretised tether to study the impact of transient effects. Instead of resolving the translational motion of the wing, we prescribe a cross-wind flight path from the flight data of Kitepower B.V. This removes the dependency of the model on the aerodynamics of the kite and, thereby, reduces uncertainties. Pertaining to the second goal, this paper provides a breakdown of the mechanisms that initiate and drive a turn of a flexible kite system with suspended control unit.

75 This paper is organised as follows. In Section 2 the experimental data underlying this study is described. In Section 3 the computational model is outlined. The results are presented in Section 4 and discussed in Section 5. Conclusions are presented in Section 6.

2 Test Flight Data

The data used in the present study was acquired on 8 October 2019 using a 25 m^2 V3.25B kite of Kitepower, depicted in Fig. 2.
80 This kite is a derivative of the TU Delft LEI V3 kite described by Oehler and Schmehl (2019) and illustrated in Fig. 3. We use the term kite for the entire assembly of the wing, bridle line system, and suspended control unit. Conservative operational settings were used for this specific flight because its purpose was to test new hard- and software components of the system and to acquire data. The operated kite was substantially smaller and less performant than the 60 m^2 kite shown in Fig. 1 that Kitepower B.V. develops for the commercial 100 kW system (Kitepower B.V.). Considering all this, the power output during the test was substantially lower than for the nominal operation of the commercial system.

Figure 2. Fully instrumented V3.25B kite before launch (photo courtesy of Kitepower B.V.).

85
The published data set (Schelbergen et al., 2023) covers approximately three hours of flight time, during which 87 automatic pumping cycles were recorded. With this large data set, statistical insights into the flight behaviour of the kite can be gained. The apparent wind speed was measured with a Pitot tube attached to the front bridle lines at the connection to a power line. This flow sensor is visible in the foreground of Fig. 2, also featuring a flow vane to measure the angle of attack. The side
90 slip angle was not measured in this setup. The onboard electrical power was supplied by a small ram-air turbine, as shown in
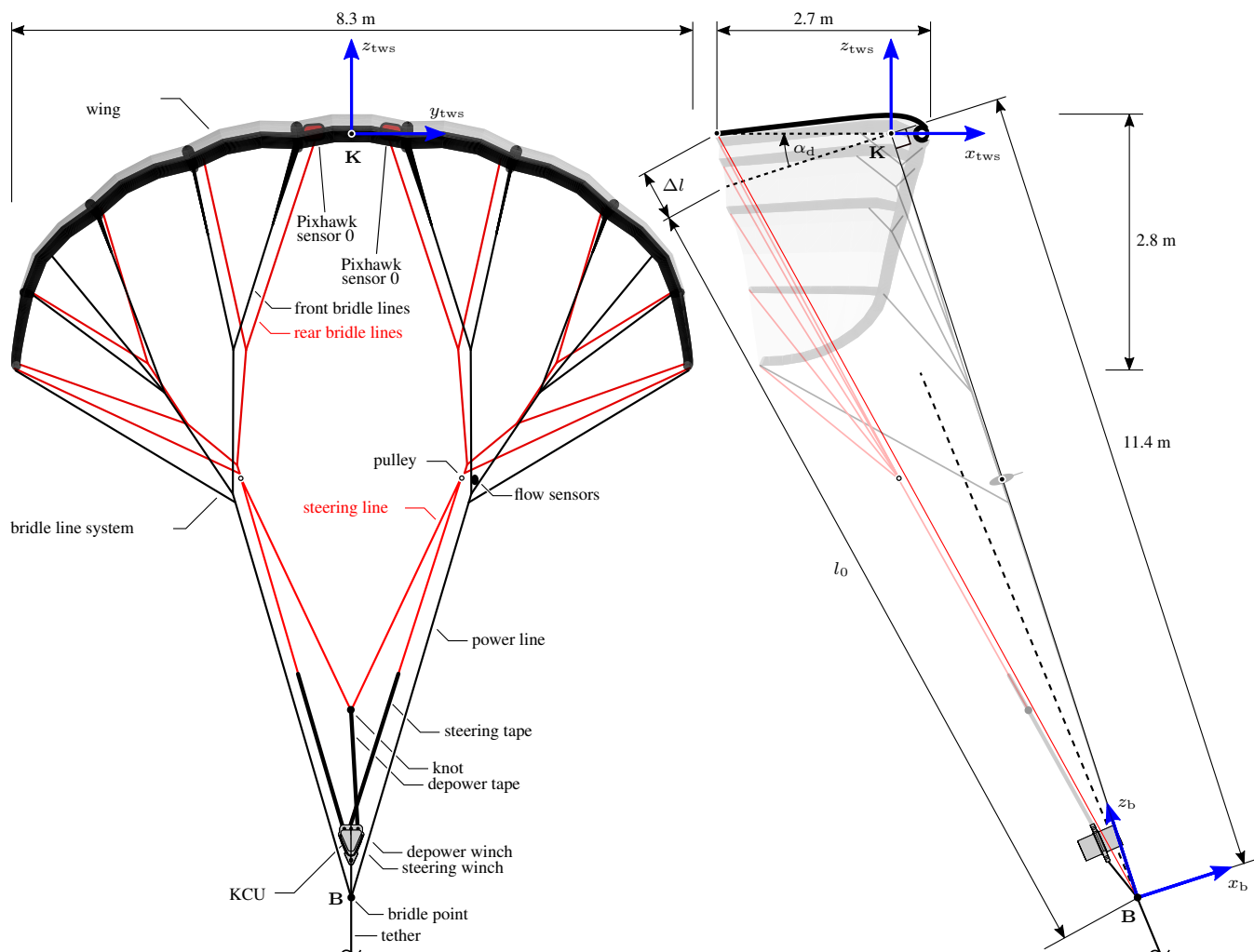
Figure 3. Front-view (left) and side-view (right) of the LEI V3 kite. Also depicted are the top wing surface (TWS) reference frame $x_{tws}, y_{tws}, z_{tws}$, with origin **K** at the point around which the wing pitches when changing the angle of attack, and the bridle reference frame x_b, y_b, z_b with origin at the bridle point **B**. The two Pixhawk® sensors 0 and 1 approximately measure in the TWS reference frame while the relative flow approximately measures in the bridle reference frame. Adapted from Oehler and Schmehl (2019).

Peschel et al. (2017). Moreover, a tether with a diameter of 10 mm was used during the flight test. The tether force and the reel-out speed were measured at the ground station.

For this flight test, two Pixhawk® sensor units were mounted to the wing, one on each of the two struts adjacent to the symmetry plane of the kite (red and green cases in Fig. 2). The units are each equipped with an IMU, GPS sensor, and barometer for recording position and attitude. Figure 4a–d depict the conditioned position data of one figure-of-eight cross-wind manoeuvre from the flight data made available by Kitepower. The position data is based on measurements of sensor 0

95

which have been processed using the default Kalman filter implementation of the Pixhawk®. The velocity measurements used in the present analysis come from the same sensor. The tangential and radial components of these measurements are depicted together with those measured by sensor 1 in Fig 4e–f (decomposition shown in Fig. 6). For an unknown reason, sensor 0 did not
100 measure acceleration. Therefore, the acceleration measured with sensor 1 is used in the analysis and is depicted in Fig. 4g–i.
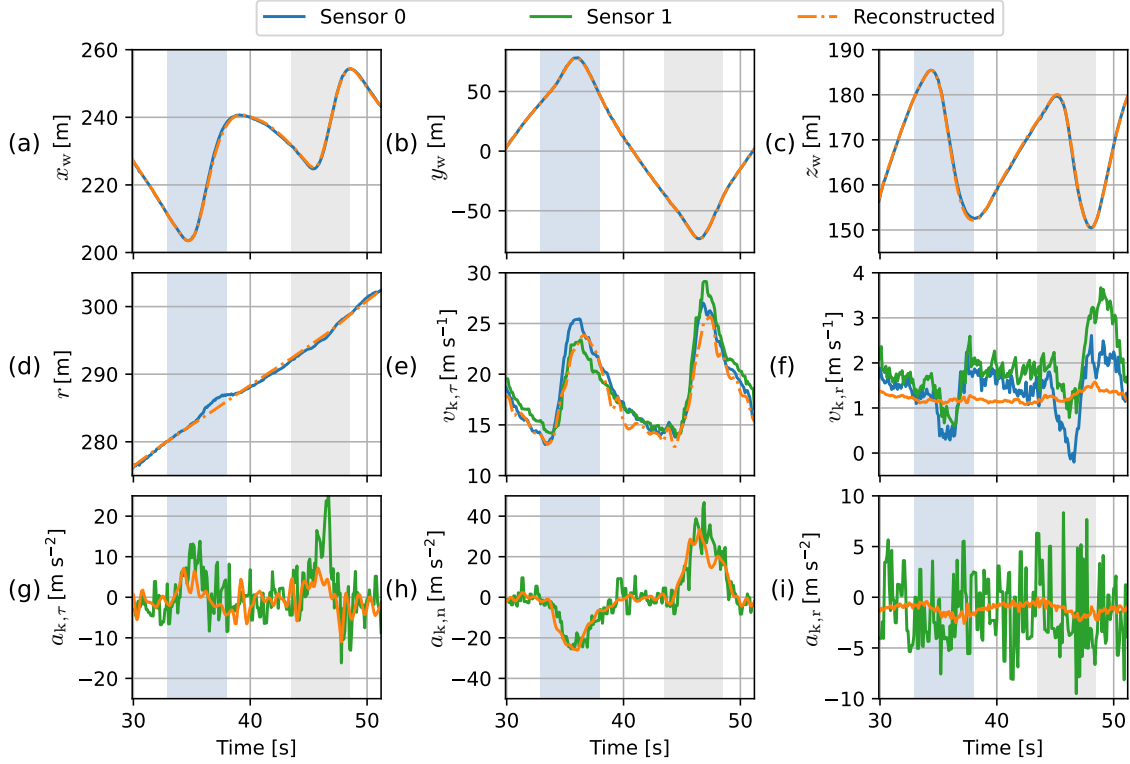
Figure 4. Kinematics of the studied figure-of-eight manoeuvre measured with the two Pixhawk® sensor units and the kinematics obtained with the flight trajectory reconstruction described in Appendix A. The intervals shaded blue and grey indicate right and left turns, respectively, from a downwind perspective. (**a–c**) Kite position coordinates of the wind reference frame (sensor data is Kalman filtered). (**d**) Radial position coordinate of the kite. (**e–f**) Tangential and radial kite velocity. (**g–i**) Tangential, normal, and radial kite acceleration.

Comparing the tether reel-out speed to the position of the wing indicates anomalies in the recorded wing position that manifest as unrealistically large jumps in radial position predominately occurring during right turns, as can be observed in Fig. 4d. These anomalies are removed using a discrete-time optimisation problem that minimises the error between the modelled radial wing speed and recorded tether reel-out speed while limiting the bias between the modelled and recorded wing position. The
105 flight trajectory reconstruction might not be strictly valid. Nevertheless, it serves the higher aim of this study by providing a consistent kinematic input for the dynamic simulation. The identification of these anomalies and the details of the optimisation are described in Appendix A.

We illustrate our analysis using a figure-of-eight cross-wind manoeuvre of the wing shown in Fig. 5. This specific manoeuvre is part of the 65th pumping cycle of the test flight. Because of the high repeatability of the automatic flight manoeuvres, the

110 other figures of eight of the dataset give similar results. Characteristic reference positions along this manoeuvre are designated to highlight the analysis, listed in Table 1. The kite flies along the trajectory in the direction of increasing reference numbers, i.e., flying upwards on the straight path segments and downwards during the turns. The tether is reeled-out while the kite is flying cross-wind manoeuvres, increasing the radial position of the kite from 276 to 302 m at a height of 150–185 m. The asymmetry of the trajectory can be attributed to various factors, including misalignment with the wind velocity due to wind

115 veer and imperfections within the system.
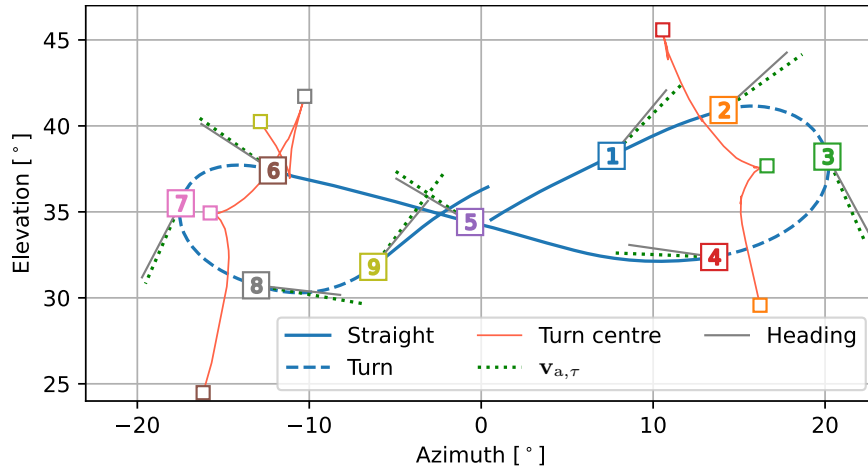
Figure 5. The studied figure-of-eight cross-wind manoeuvre of the wing depicted with respect to the wind reference frame, shown in Fig. B1. The flight path is composed of straight (solid blue) and turn (dashed blue) line segments. Reference positions 1 to 9 are designated along the path in flight direction. For the two turns, the changing position of the turn centre is tracked with the red lines. The turn-centre markers pair with the numbered path markers of the same colour. The dotted lines depict the modelled tangential apparent wind velocity. Alongside the apparent wind velocity lines, the solid lines depict the heading inferred from the attitude measurements of sensor 1.

Table 1. Timestamps of the reference positions along the figure-of-eight path shown in Fig. 5, starting at 29.9 s and ending at 51.2 s in the 65th pumping cycle.

Instance label	1	2	3	4	5	6	7	8	9
Time [s]	31.9	33.9	35.6	37.5	41.0	44.5	46.2	47.6	49.1

For simplicity, the present study assumes that the wind velocity is uniform and constant. The average wind speed measured at the ground for the reference pumping cycle is approximately 7 m s^{-1}. Based on the estimated wind shear, the wind speed at the kite is assumed to be 10 m s^{-1}. The grey lines in Fig. 5 show the heading of the kite at the reference positions inferred

from sensor 1. The dotted green lines show the projection of the apparent wind velocity approximated with

120 $$\mathbf{v}_a = \mathbf{v}_\mathrm{w} - \mathbf{v}_\mathrm{k}\,, \tag{1}$$

in which $\mathbf{v}_\mathrm{w} = [10\,0\,0]^\top$ is the wind velocity and $\mathbf{v}_\mathrm{k}$ is the measured kite velocity. The side slip angle is the angle between the heading of the kite and the apparent wind velocity. The approximation of the apparent wind velocity lacks the necessary precision to assess the side slip. Moreover, the side slip angle was not measured during the flight test and, therefore, assessing the side slip is out of scope.

125 ## 3 Computational Modelling

The flight behaviour along the figure of eight described in the previous section is analysed with two different methods for solving the motion of the two-point kite model with a discretised tether model. First, this section discusses the tether-kite model configuration. Next, the two methods for solving the motion are discussed. The first approximates the tether-kite motion as a transition through steady-rotation states. The second solves the motion directly with dynamic equations of motion.

130 ### 3.1 Tether-kite model

The two-point kite model accounts for the two distinct mass concentrations of the wing and the KCU. During cross-wind flight, the bridle line system is tensioned by the aerodynamic force acting on the wing. Accordingly, the two point masses stay at a constant distance, considering that the effect of wing actuation, including deformation, is negligible. From a modelling perspective, the two point masses at a constant distance are similar to a rigid body model, with rotational inertia in pitch and

135 roll, but not in yaw. The yaw motion is irrelevant for the present analysis due to the exclusion of the wing aerodynamics. This would not be the case when solving the full, unconstrained kite motion.

The two-point kite model developed for the present analysis can be added in a straightforward way to a discretised tether model as an additional final segment. An example with five tether segments of equal length l_j and a kite segment of length l_b is shown in Fig. 6.

140 To account for a varying length l_t and mass m_t of the deployed tether, the segment lengths and point masses are updated every instance according to

$$l_\mathrm{j} = \frac{l_\mathrm{t}}{N}, \tag{2}$$

$$m_\mathrm{j} = \frac{m_\mathrm{t}}{N}, \tag{3}$$

where N is the constant number of tether elements. The point mass representing the KCU is determined as

145 $$m'_\mathrm{kcu} = m_\mathrm{kcu} + \frac{m_\mathrm{j}}{2}. \tag{4}$$

The tether and bridle segments are assumed to be rigid. Moreover, variations in the lengths of these segments due to elasticity are neglected. The effect of tether elasticity on the swinging motion of the kite is expected to be negligible as long as the modelled tether length agrees with the effective real-world tether length.
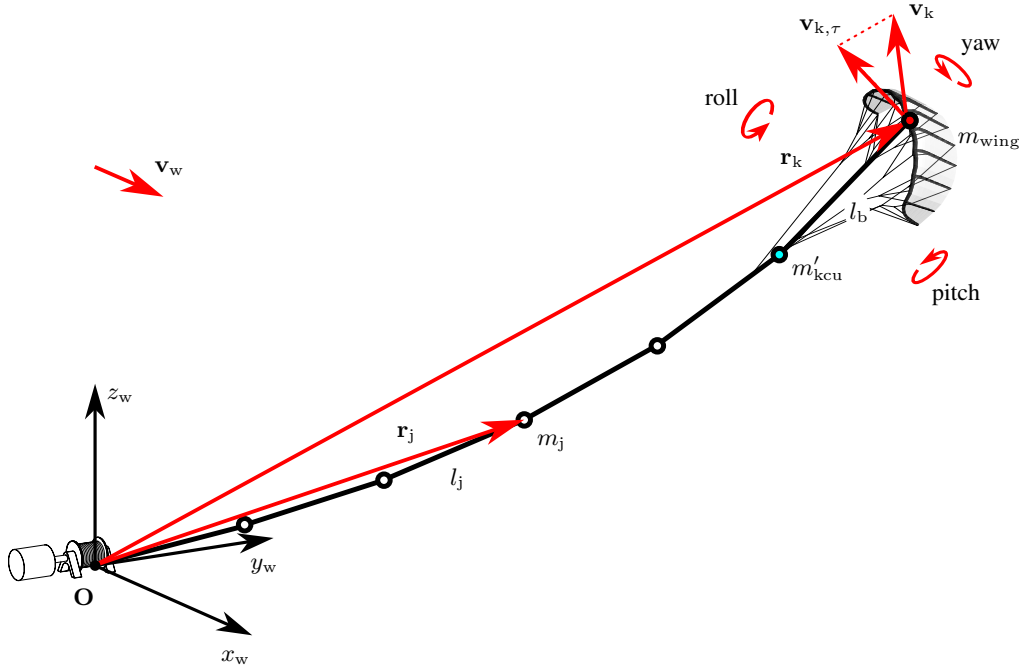
Figure 6. Two-point model of the kite added to a tether discretised by $N = 5$ tether elements. The position $\mathbf{r}_\mathrm{k}$ and flight velocity $\mathbf{v}_\mathrm{k}$ of the kite are defined as the position and velocity of the point $\mathbf{S}$ where the sensor units are attached to the wing, see Figure 4. Also shown is the tangential kite velocity component $\mathbf{v}_{\mathrm{k},\tau}$ (perpendicular to $\mathbf{r}_\mathrm{k}$) and the wind reference frame $x_\mathrm{w}, y_\mathrm{w}, z_\mathrm{w}$ with origin at the tether attachment point $\mathbf{O}$ on the ground and x_w-axis aligned with the wind velocity vector.

Aerodynamic drag is one of the forces considered to act on the point masses representing the tether. The drag is calculated as

$$\mathbf{D}_{\mathrm{t},\mathrm{j}} = \frac{1}{2} \rho \|\mathbf{v}_{\mathrm{a}\perp,\mathrm{j}}\| \, \mathbf{v}_{\mathrm{a}\perp,\mathrm{j}} \, C_{\mathrm{D},\mathrm{t}} \, l_\mathrm{j} \, d_\mathrm{t} , \qquad \text{with} \quad j = 1,\dots,N, \tag{5}$$

where ρ is the air density, $\mathbf{v}_{\mathrm{a}\perp,\mathrm{j}}$ is the local apparent wind velocity perpendicular the tether segment below the jth point mass, $C_{\mathrm{D},\mathrm{t}}$ is the tether drag coefficient, and d_t is the tether diameter.

Two aerodynamic forces are acting on the KCU point mass below the wing: the drag of the KCU itself $\mathbf{D}_{\mathrm{kcu}}$ and half the drag of the upper tether element. Consequently, the total drag acting on the KCU point mass is

$$\mathbf{D}'_{\mathrm{kcu}} = \mathbf{D}_{\mathrm{kcu}} + \mathbf{D}_{\mathrm{t},\mathrm{kcu}} = \frac{1}{2} \rho \|\mathbf{v}_{\mathrm{a}\perp,\mathrm{kcu}}\| \, \mathbf{v}_{\mathrm{a}\perp,\mathrm{kcu}} \, C_{\mathrm{D},\mathrm{kcu}} \, A_{\mathrm{kcu}} + \frac{\mathbf{D}_{\mathrm{t},\mathrm{N}}}{2} , \tag{6}$$

in which $\mathbf{v}_{\mathrm{a}\perp,\mathrm{kcu}}$ is the perpendicular component of the apparent wind velocity at the KCU. The frontal area of the KCU is denoted as A_{kcu} and the drag coefficient as $C_{\mathrm{D},\mathrm{kcu}}$. The chosen value of 1.0 for the drag coefficient is within the common range for a blunt body. The bridle and ram-air turbine drag are not included as separate terms but are considered accounted for by the KCU and wing drag. The values of physical parameters are listed in Table 2.

Table 2. Physical parameters of the airborne system model.

v_w	m_{kcu}	m_{wing}	l_b	ρ	d_t	$C_{D,t}$	A_{kcu}	$C_{D,kcu}$
$10\ \mathrm{m\,s^{-1}}$	25 kg	14.2 kg	11.5 m	$1.225\ \mathrm{kg\,m^{-3}}$	10 mm	1.1	$0.25\ \mathrm{m^2}$	1.0

Equation (5) does not account for any variation of the apparent wind velocity along the tether element and is only a reasonable approximation when using many tether elements. For single-element use, the alternative expression for the tether drag contribution (last term in Eq. (6)) better preserves the moment of the tether drag around the ground station

$$\mathbf{D}_{t,kcu} = \frac{1}{8}\,\rho\,\|\mathbf{v}_{a\perp,kcu}\|\,\mathbf{v}_{a\perp,kcu}\,C_{D,t}\,l_t\,d_t\,. \tag{7}$$

165 **3.2 Steady-rotation state**

The subroutine for solving the 'quasi-static' tether shape proposed by Williams (2017) is adopted in the present analysis to assess the swinging motion of the kite. With an initial guess of the tether length and orientation of the lower segment, the corresponding tether shape is determined using a shooting method. The positions of the point masses are determined one by one, starting with the lowest point mass and moving up towards the last point mass located at the tether end. From the pseudo

170 force balance on a particular point mass (at the intersection of two tether elements), the position of the next point mass is inferred. This balance considers the tensile forces, drag, weight, and centrifugal force. Given the tensile force acting on the tether element below the point mass, only the tensile force acting on the tether element above remains unknown and is solved. The direction of this force dictates the axial direction of the corresponding tether element. Together with the length of a tether element, the axial direction yields the position of the next point mass. By repeating this calculation for each point mass, the

175 position of the kite is obtained given the measured tether force at the ground. A least squares optimisation is employed to find the tether length and shape for which the upper tether end coincides with the position of the wing. Consult Williams (2017) for more details.

To facilitate the calculation of loads, the velocities and accelerations of the point masses are approximated by assuming that they collectively rotate around the tether attachment point at the ground with a constant angular velocity $\boldsymbol{\omega}$, treating the point

180 masses as particles lying on a rigid body. According to this kinematic assumption, the velocity and acceleration of each point mass depend solely on the angular velocity and its respective position. The velocity $\mathbf{v}_j$ and acceleration $\mathbf{a}_j$ for the jth point mass are

$$\mathbf{v}_j = \boldsymbol{\omega} \times \mathbf{r}_j\,, \qquad \text{with} \quad j = 1,\ldots,N \tag{8}$$

$$\mathbf{a}_j = \boldsymbol{\omega} \times \mathbf{v}_j\,, \qquad \text{with} \quad j = 1,\ldots,N \tag{9}$$

185 where $\mathbf{r}_j$ is the position of the point mass. This kinematic assumption is referred to as the steady-rotation assumption throughout this paper.

Prior to calculating the kinematics of the point masses, the angular velocity needs to be determined. Williams approximates the rotational velocity with

$$\boldsymbol{\omega}_{\text{straight}} = \frac{\mathbf{r}_k \times \mathbf{v}_k}{\|\mathbf{r}_k\|^2} = \frac{\mathbf{r}_k \times \mathbf{v}_{k,\tau}}{\|\mathbf{r}_k\|^2}, \tag{10}$$

190 in which $\mathbf{r}_k$ and $\mathbf{v}_k$ are the position and velocity of the kite, respectively, and $\mathbf{v}_{k,\tau}$ is the tangential component of the kite velocity, shown in Fig. 6. The resulting rotational velocity yields a rotation along a great circle on the surface of a sphere, as shown in Fig. 7. This rotational velocity is labelled as 'straight', because the great-circle rotation produces the straight path segments of a figure-of-eight manoeuvre. Note that this rotational velocity is perpendicular to the position and the (tangential) velocity of the kite, i.e., it points into the normal direction.

195 A shortcoming of this great-circle angular velocity approximation is that it does not yield an acceleration representative for a turning kite. Calculating the corresponding acceleration according to the steady-rotation assumption (Eqs. (8) and (9)) will yield an acceleration that is aligned with the position vector and, thus, no lateral acceleration. The lateral acceleration, however, is important to consider as it is the dominant component during turns, as can be observed in Fig. 4h. The kinematic assumption does allow a lateral acceleration, however, this requires that the angular velocity has a radial component. Note that

200 the steady-rotation assumption cannot produce a tangential acceleration.

The addition of a radial component to the great-circle angular velocity approximation enables producing a rotation along a small circle on the surface of a sphere coinciding with the turn of the figure-of-eight manoeuvre as shown in Fig. 7. Similar to the derivation of the normal angular velocity from Eq. (8), the radial angular velocity is derived from Eq. (9) and can be calculated with the normal component of the acceleration $\mathbf{a}_{k,n}$:

$$205 \quad \boldsymbol{\omega}_{\text{r}} = \frac{\mathbf{v}_{k,\tau} \times \mathbf{a}_{k,n}}{\|\mathbf{v}_{k,\tau}\|^2}. \tag{11}$$

The newly proposed rotational velocity approximation for turns reads as:

$$\boldsymbol{\omega}_{\text{turn}} = \boldsymbol{\omega}_{\text{straight}} + \boldsymbol{\omega}_{\text{r}}. \tag{12}$$

The wing kinematics resulting from the flight path reconstruction are used to calculate the rotational velocity for turns. Figure 8a shows that the normal component of the turn rotational velocity is much smaller than the radial component. Fig-
210 ure 8b-c show the kinematics back-calculated with the steady-rotation assumption. The back-calculated wing velocity is solely produced by the normal component of the turn rotational velocity and only has a tangential component. Although the original wing velocity does have a radial component (smaller than $1.6\,\mathrm{m\,s^{-1}}$) and the back-calculated speed does not, their magnitudes are virtually the same. In contrast, the back-calculated wing acceleration is solely produced by the large radial component of the turn rotational velocity. The back-calculated wing acceleration also shows a very good match with the original wing
215 acceleration despite that it does not have a tangential component. In conclusion, these results show that the steady-rotation assumption yields a very good approximation of the kite kinematics.

To conclude, we incorporate the following model modifications with respect to the model of Williams (2017):

– The elasticity of the tether elements is not considered as ;
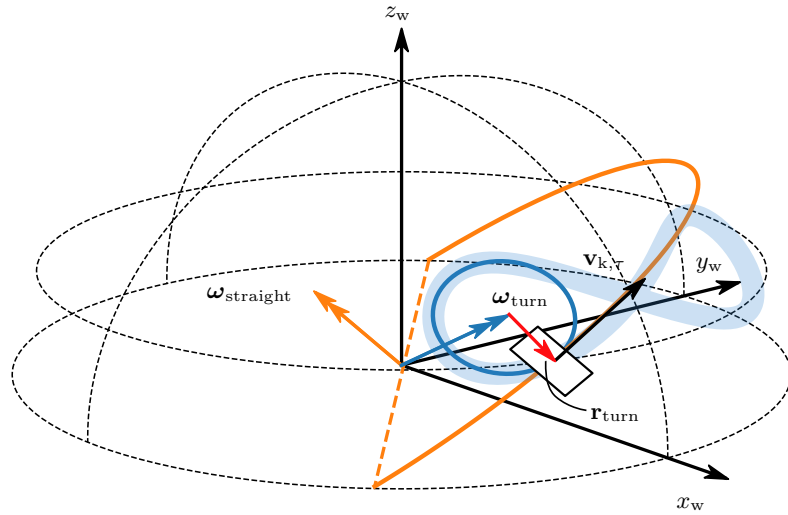
Figure 7. Two possible angular velocities, $\boldsymbol{\omega}_{\text{straight}}$ and $\boldsymbol{\omega}_{\text{turn}}$, that can be deduced from the tangential kite velocity $\mathbf{v}_{\text{k},\tau}$. Their respective steady-rotation flight paths comprise a great circle (orange) and an instantaneous turn circle (blue) that approximately coincides with the turn of the figure-of-eight manoeuvre. The yawed tangential plane perpendicular to the position vector of the kite is depicted as a rectangle and represents the kite.

    – We add a radial component to the great-circle angular velocity;

    – A different lumping approach is used for the uppermost tether point mass than for the other tether point masses, i.e., the mass and drag of half a tether element are allocated to the former instead of the mass and drag of a full element;

    – We add an extra element (rigid link) to represent the kite as described in Section 3.1.

3.3 Dynamic equations of motion

The proposed dynamic model is a derivative of the generic model for multiple kite system architectures with fixed tether lengths introduced by Zanon et al. (2013). This model uses Cartesian coordinates to reduce the non-linearity of the model formulation. Although the model allows for complex systems, we only consider a simple single-tether, single-kite configuration. To limit the dimensions of the presented system of equations, we introduce a two-point kite model formulation with only two tether elements, in contrast to the 30 tether elements used for generating results. The first tether element connects the ground station to the only designated tether point mass m_1, and the second tether element connects m_1 to the point mass of the control unit m'_{kcu}, in a similar arrangement as the configuration depicted in Fig. 6.

The model is described by a differential-algebraic system of equations (DAE), with constraints originating from the use of non-minimal coordinates. The differential states $\mathbf{x}$, algebraic states $\mathbf{z}$, and control inputs $\mathbf{u}$ of the two-point model are

$$\mathbf{x} = [\mathbf{r}_1,\, \mathbf{r}_{\text{kcu}},\, \mathbf{r}_\text{k},\, \mathbf{v}_1,\, \mathbf{v}_{\text{kcu}},\, \mathbf{v}_\text{k},\, l_\text{t},\, \dot{l}_\text{t}], \quad \mathbf{z} = [\mathbf{a}_1,\, \mathbf{a}_{\text{kcu}},\, \lambda_1,\, \lambda_2,\, \lambda_\text{b}], \quad \text{and} \quad \mathbf{u} = [\mathbf{a}_\text{k},\, \ddot{l}_\text{t}]; \tag{13}$$
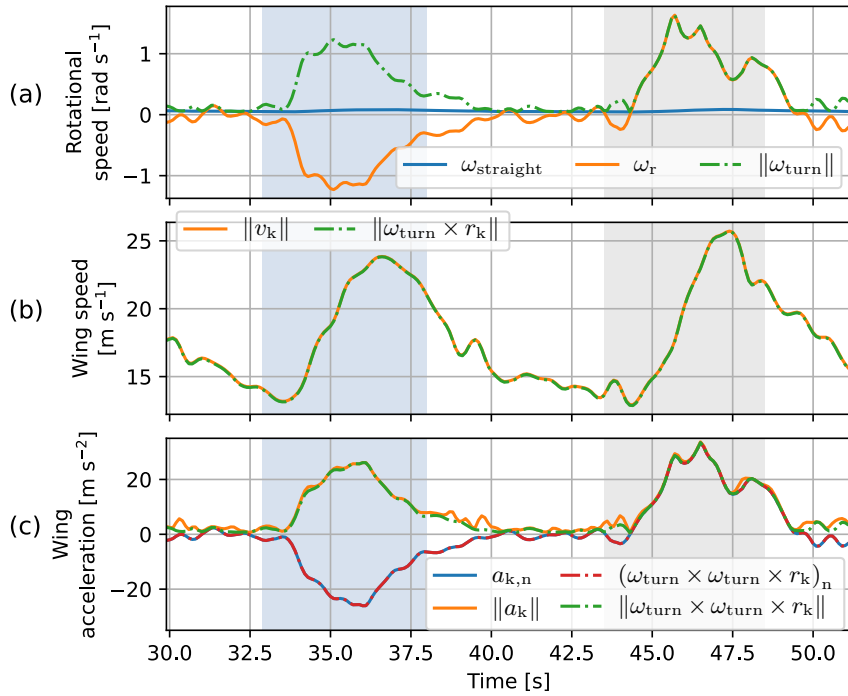
Figure 8. Assessing the steady-rotation assumption with the rotational velocity for turns. (**a**) The normal (straight-path) and radial rotational speed inferred from the reconstructed wing kinematics. (**b**, **c**) The wing speed and acceleration back-calculated with the turn rotational velocity (using Eqs. (8) and (9)) compared to the wing speed and acceleration from the flight trajectory reconstruction used to calculate the rotational velocity. The shaded intervals indicate the turns.

in which subscript kcu refers to the kite control unit, k refers to the top wing surface of the kite, t denotes tether, b denotes bridle, and the numbers refer to the tether point masses and elements. The state variables are the positions and velocities of the point masses and the tether length and reel-out speed. The algebraic variables include the acceleration of the control unit point mass and Lagrange multipliers λ. The Lagrange multipliers enforce the constraints and have a close relationship with the forces acting in the tether and bridle elements. The control variables are the wing acceleration and the reel-out acceleration of the tether.

Without imposing the translational motion of the wing, the dynamics of the two-point kite model with two tether elements read as:

$$
\begin{bmatrix}
\begin{bmatrix}
m_1\mathbf{I}_3 & \mathbf{0}_{3\times3} & \mathbf{0}_{3\times3} \\
\mathbf{0}_{3\times3} & m'_{\text{kcu}}\mathbf{I}_3 & \mathbf{0}_{3\times3} \\
\mathbf{0}_{3\times3} & \mathbf{0}_{3\times3} & m_k\mathbf{I}_3
\end{bmatrix} & \mathbf{G}_X^\top \\
\mathbf{G}_X & \mathbf{0}_{3\times3}
\end{bmatrix}
\begin{bmatrix}
\mathbf{a}_1 \\
\mathbf{a}_{\text{kcu}} \\
\mathbf{a}_k \\
\lambda_1 \\
\lambda_2 \\
\lambda_b
\end{bmatrix}
=
\begin{bmatrix}
\mathbf{D}_{\text{t},1} - m_1\,g\,\mathbf{1}_z \\
\mathbf{D}'_{\text{kcu}} - m'_{\text{kcu}}\,g\,\mathbf{1}_z \\
\mathbf{F}_a - m_k\,g\,\mathbf{1}_z \\
-\mathbf{v}_1^\top\mathbf{v}_1 + \frac{1}{N^2}\left(\dot{l}_t^{\,2} + l_t\ddot{l}_t\right) \\
-\left(\mathbf{v}_{\text{kcu}} - \mathbf{v}_1\right)^\top\left(\mathbf{v}_{\text{kcu}} - \mathbf{v}_1\right) + \frac{1}{N^2}\left(\dot{l}_t^{\,2} + l_t\ddot{l}_t\right) \\
-\left(\mathbf{v}_k - \mathbf{v}_{\text{kcu}}\right)^\top\left(\mathbf{v}_k - \mathbf{v}_{\text{kcu}}\right)
\end{bmatrix}
\tag{14}
$$

in which

$$
\mathbf{G}_X =
\begin{bmatrix}
\mathbf{r}_1 & \mathbf{0}_{1\times3} & \mathbf{0}_{1\times3} \\
(\mathbf{r}_1 - \mathbf{r}_{\text{kcu}})^\top & (\mathbf{r}_{\text{kcu}} - \mathbf{r}_1)^\top & \mathbf{0}_{1\times3} \\
\mathbf{0}_{1\times3} & (\mathbf{r}_{\text{kcu}} - \mathbf{r}_k)^\top & (\mathbf{r}_k - \mathbf{r}_{\text{kcu}})^\top
\end{bmatrix},
\tag{15}
$$

$\mathbf{I}_3$ is the identity matrix, $\mathbf{F}_a$ is the aerodynamic force acting on the wing, g is the gravitational constant, and $\mathbf{1}_z = [0\ 0\ 1]^\top$. The equations of motion for the point masses are described in the upper three rows. The constraint equations described in the lower three rows represent the links between the point masses.

The constraint equations in the lower three rows of Eq. (14) are inferred from the constraints on the distances between linked point masses. The distance between the control unit and the top wing surface point masses is constrained by the constant bridle length l_b:

$$
c_b = \frac{1}{2}\left((\mathbf{r}_k - \mathbf{r}_{\text{kcu}})^\top(\mathbf{r}_k - \mathbf{r}_{\text{kcu}}) - l_b^2\right) = 0.
\tag{16}
$$

The relative distances between the remaining linked point masses are constraint by the instantaneous tether length l_t:

$$
c_1 = \frac{1}{2}\left(\mathbf{r}_1^\top\mathbf{r}_1 - \left(\frac{l_t}{N}\right)^2\right) = 0
\tag{17}
$$

and

$$
c_2 = \frac{1}{2}\left((\mathbf{r}_{\text{kcu}} - \mathbf{r}_1)^\top(\mathbf{r}_{\text{kcu}} - \mathbf{r}_1) - \left(\frac{l_t}{N}\right)^2\right) = 0.
\tag{18}
$$

These constraints are differentiated twice to yield an index-1 DAE, enabling more efficient integration. As a consequence of the index reduction, the tether length acceleration and the accelerations of the point masses appear in the constraint equations. The initial states must satisfy two consistency conditions per constraint to ensure consistent kinematics of the tether and point masses in the simulation. The original expressions for the constraints serve as consistency conditions. Moreover, the time derivatives of these expressions are required as consistency conditions:

$$
\dot{c}_b = (\mathbf{r}_k - \mathbf{r}_{\text{kcu}})^\top(\mathbf{v}_k - \mathbf{v}_{\text{kcu}}) = 0,
\tag{19}
$$

$$\dot{c}_1 = \mathbf{r}_1^\top \mathbf{v}_1 - \frac{l_t \dot{l}_t}{N^2} = 0 \tag{20}$$

and

$$\dot{c}_2 = (\mathbf{r}_{kcu} - \mathbf{r}_1)^\top (\mathbf{v}_{kcu} - \mathbf{v}_1) - \frac{l_t \dot{l}_t}{N^2} = 0. \tag{21}$$

To prevent inaccuracies of an aerodynamic model of the wing interfering with the simulation, we do not resolve the dynamics of the point mass of the wing. Instead, the acceleration of the wing is prescribed and used as input. The wing acceleration is inferred from a cross-wind flight path from the flight data of Kitepower B.V., as described in Appendix A. Consequently, the equation of motion of the wing (third row in Eq. (14)) becomes redundant and is dropped for this analysis:

$$\begin{bmatrix} \begin{bmatrix} m_1 \mathbf{I}_3 & \mathbf{0}_{3\times3} \\ \mathbf{0}_{3\times3} & m'_{kcu} \mathbf{I}_3 \end{bmatrix} & \mathbf{G}'^\top_X \\ \mathbf{G}'_X & \mathbf{0}_{3\times3} \end{bmatrix} \begin{bmatrix} \mathbf{a}_1 \\ \mathbf{a}_{kcu} \\ \lambda_1 \\ \lambda_2 \\ \lambda_b \end{bmatrix} = \begin{bmatrix} \mathbf{D}_{t,1} - m_1 g \mathbf{1}_z \\ \mathbf{D}'_{kcu} - m'_{kcu} g \mathbf{1}_z \\ -\mathbf{v}_1^\top \mathbf{v}_1 + \frac{1}{N^2}\left(\dot{l}_t^2 + l_t \ddot{l}_t\right) \\ -(\mathbf{v}_{kcu} - \mathbf{v}_1)^\top (\mathbf{v}_{kcu} - \mathbf{v}_1) + \frac{1}{N^2}\left(\dot{l}_t^2 + l_t \ddot{l}_t\right) \\ -(\mathbf{v}_k - \mathbf{v}_{kcu})^\top (\mathbf{v}_k - \mathbf{v}_{kcu}) - (\mathbf{r}_k - \mathbf{r}_{kcu})^\top \mathbf{a}_k \end{bmatrix} \tag{22}$$

in which $\mathbf{G}'_X$ is Eq. (15) with the third column removed. Moreover, the term with the wing acceleration in the algebraic equation of the bridle element is moved to the right-hand side.

Incorporating the acceleration of the control unit point mass as an algebraic state allows the DAE of the full model to be expressed in a semi-explicit form. The time derivatives of the differential states are

$$\dot{\mathbf{x}} = [\mathbf{v}_1, \ \mathbf{v}_{kcu}, \ \mathbf{v}_k, \ \mathbf{a}_1, \ \mathbf{a}_{kcu}, \ \mathbf{a}_k, \ \dot{l}_t, \ \ddot{l}_t] \tag{23}$$

and the algebraic equations are obtained by rearranging Eq. (22). The DAE is solved with the IDAS integrator in CasADi (Andersson et al., 2019). IDAS employs the backward differentiation formula (variable-order, variable-coefficient) for implicit integration to solve the system. The motion is resolved at a fixed time step of 0.1 s. The solver produces a consistent simulation with insignificant drift in the consistency conditions, i.e., the distance between the wing and the KCU drifts with 0.0001 m in 24.2 s.

In contrast to the steady-rotation state calculation in Sec. 3.2, drag is calculated directly with the local apparent wind velocity $\mathbf{v}_{a,j}$ instead of its normal component $\mathbf{v}_{a\perp,j}$ (Eqs. (5), (6), and (7)) to limit the non-linearity of the model. To sum up, we incorporate the following model modifications with respect to the work of Zanon et al. (2013):

– The tether length time derivatives are added to the dynamic equations to enable modelling pumping AWE systems;

– Drag is computed directly at the point masses instead of being computed at the centers of the tether elements and then lumped to the adjacent point masses;

– The acceleration of the top of the kite (wing point mass) is not solved for. Instead, the wing acceleration inferred from measurements is directly imposed;

– Also here, we add an extra element (rigid link) to represent the kite as described in Section 3.1.

4 Results

Firstly, the steady-rotation-state approximation is used to study the motion of the tether and kite along the figure of eight. A discretisation by 30 tether segments is compared with a minimal discretisation using only a single tether segment. Secondly, the motion is simulated with the dynamic model using 30 tether segments. Subsequently, the resulting roll and pitch along the figure of eight from the different models are compared with measurements. Finally, the motion of the tether and kite along a full pumping cycle is studied.

4.1 Tether-kite lines computed with steady-rotation states

The steady-rotation-state approximation uses the measured tether force, wing position, and optimised angular velocity to determine the instantaneous positions of the point masses. The line formed by the segments between these point masses is referred to as the tether-kite line. Figure 9 shows the resulting tether-kite lines with 30 tether elements at the reference instances.
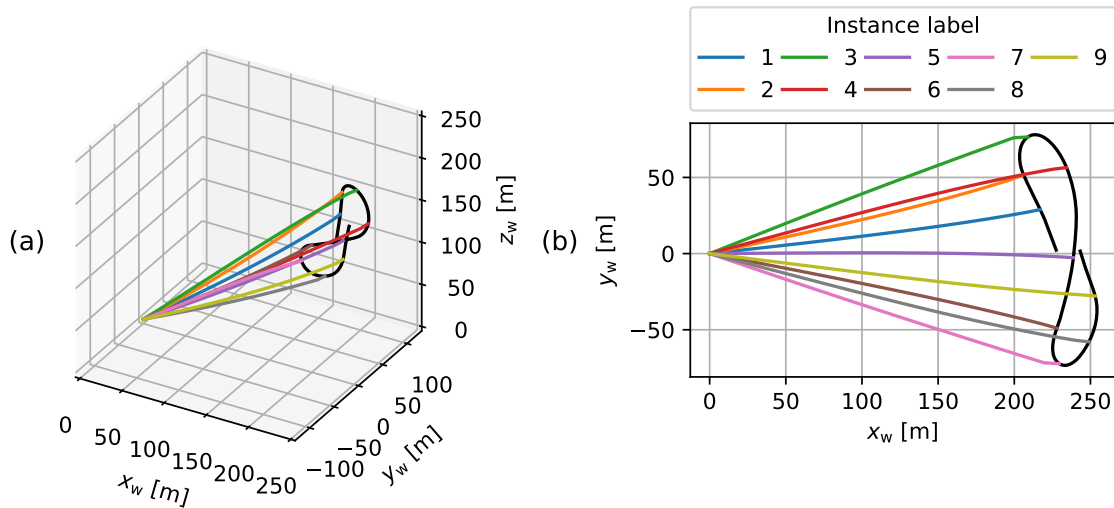
Figure 9. Tether-kite lines for the nine reference instances resulting from the steady-rotation-state approximation with the tether discretised by 30 segments in 3D (**a**) and top-view (**b**).

Variations in the deformation of the tether-kite line are hard to identify with the naked eye in the previous plots. Therefore, the cross-axial displacement is plotted against the radial position for the first five reference instances with the solid lines in Fig. 10. The displacement is expressed with respect to the tangential apparent wind velocity of the kite. The largest displacements are found in the down-apparent-wind direction, which can be attributed to the tether drag. The direction in which gravity contributes

305   to the displacement varies depending on the position along the figure of eight. Table 3 specifies in which direction gravity acts for the first five reference instances. For all instances except for the third, gravity acts in the down-apparent-wind direction. The cross-apparent-wind displacement contribution of gravity changes sign after the third instance. Finally, the resistance to turn, or the inertia, mostly contributes to the displacement in the positive cross-apparent-wind direction, as can be inferred from the high positive values in the last column of Table 3.
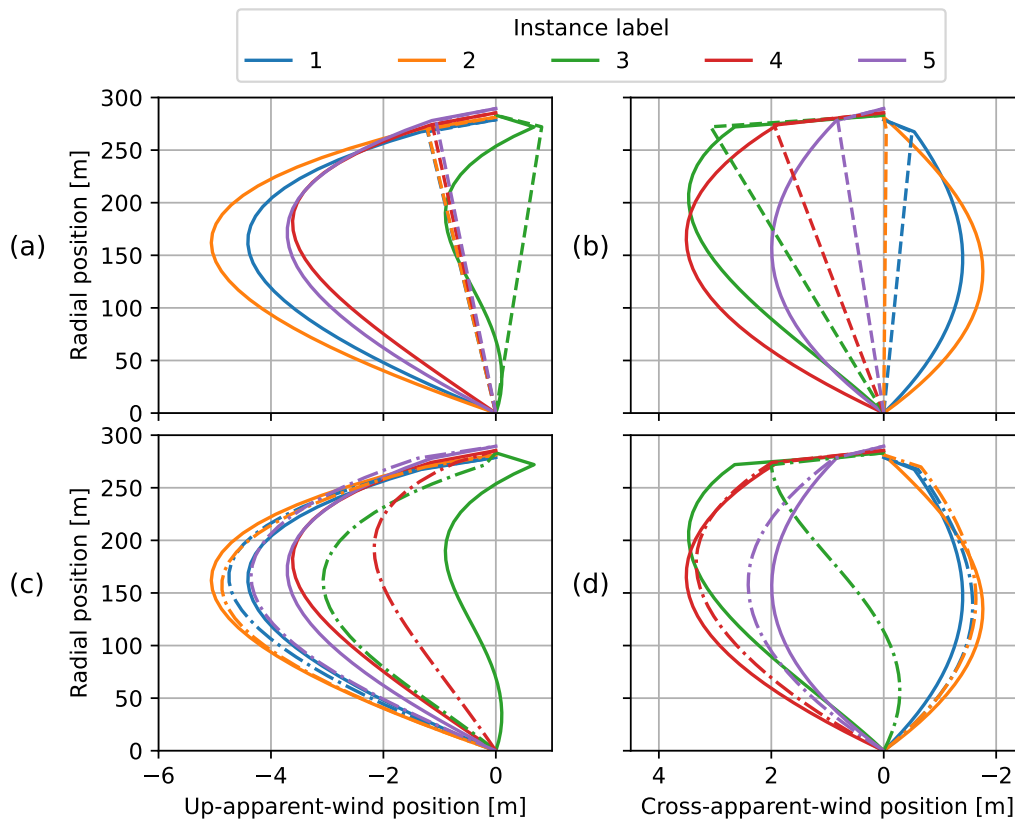
Figure 10. Tether-kite lines with cross-axial displacement decomposed with respect to the tangential apparent wind velocity of the wing (see Fig. 5). Steady-rotation states with 30 tether elements (solid lines in **a**, **b**, **c**, and **d**), with a single tether element (dashed lines in **a** and **b**), and the dynamic solution with 30 tether elements (dash-dotted lines in **c** and **d**) for the first five reference instances. Note that the x- and y-axes have different scales and that the x-axes are flipped in the second column.

Table 3. The negated vertical unit vector $-\mathbf{1}_z$ and the negated centripetal unit vector $-\mathbf{e}_{\text{centripetal}}$ decomposed in the up-apparent-wind and cross-apparent-wind direction experienced by the wing. The centripetal unit vector is determined by the approximated centripetal acceleration at the kite $\mathbf{e}_{\text{centripetal}} = \frac{\boldsymbol{\omega}_{\text{turn}} \times (\boldsymbol{\omega}_{\text{turn}} \times \boldsymbol{r}_k)}{\|\boldsymbol{\omega}_{\text{turn}} \times (\boldsymbol{\omega}_{\text{turn}} \times \boldsymbol{r}_k)\|}$. The listed fractions help to explain the contributions of gravity and turn inertia to the cross-axial displacement of the tether-kite lines in Fig. 10.

	$-\mathbf{1}_z$		$-\mathbf{e}_{\text{centripetal}}$	
Instance label	Up	Cross	Up	Cross
1	-0.56	-0.55	0.09	0.41
2	-0.44	-0.62	0.28	0.95
3	0.72	-0.32	0.25	0.97
4	-0.03	0.84	-0.23	0.96
5	-0.46	0.68	-0.27	0.84

The discontinuities in the tether-kite lines at the KCU indicate that it has a substantial effect on the attitude of the kite element. These discontinuities are caused by the high mass and drag that are allocated to the KCU point relative to those lumped to the tether points.

To illustrate the imposed kite attitude more clearly, it is quantified using the pitch and roll of the kite element with respect to the tangential plane (perpendicular to the position vector of the kite). The exact definitions are given in Appendix B. Figure 11a shows that the pitch is roughly constant during the straight flight path sections and drops below zero during the turns (blue line). The negative pitch is confirmed by the tether-kite line plot of the 3rd instance in Fig. 10a, where the upper kite element is tilted backwards. Note that this depiction changes when plotting the tether-kite line with respect to, e.g., the vertical instead of the apparent wind velocity. The KCU is actually positioned higher than the wing and can be considered to be pulled along by the wing.

Figure 11b shows a distinct pattern for the roll of the kite along the figure of eight (blue line). The roll is slightly negative, roughly constant at the first straight section flying to the right, whereas it is slightly positive at the subsequent straight section flying to the left. In between, during the right turn, the roll peaks in the middle of the turn at 36.2 s. The left turn shows an opposite pattern. Note that the model does not account for transient effects, which are expected to be substantial during the turns.

The rolling motion of the kite during the turns can be predominantly attributed to the resistance to turn, or inertia, of the KCU. The inertia of the tether has a much smaller effect on the roll. This stresses the need for including a separate point mass for the KCU when assessing the kite attitude.

The analysis is repeated using a single tether element. Figure 10a and b show the resulting tether-kite lines with the dashed lines. As expected, this minimal model is not able to give a good estimation of the maximum displacements. Nevertheless, the resulting kite elements align well with the results of the model with 30 tether elements. Figure 11 confirms this alignment as both the pitch and roll are similar for the two discretisations.
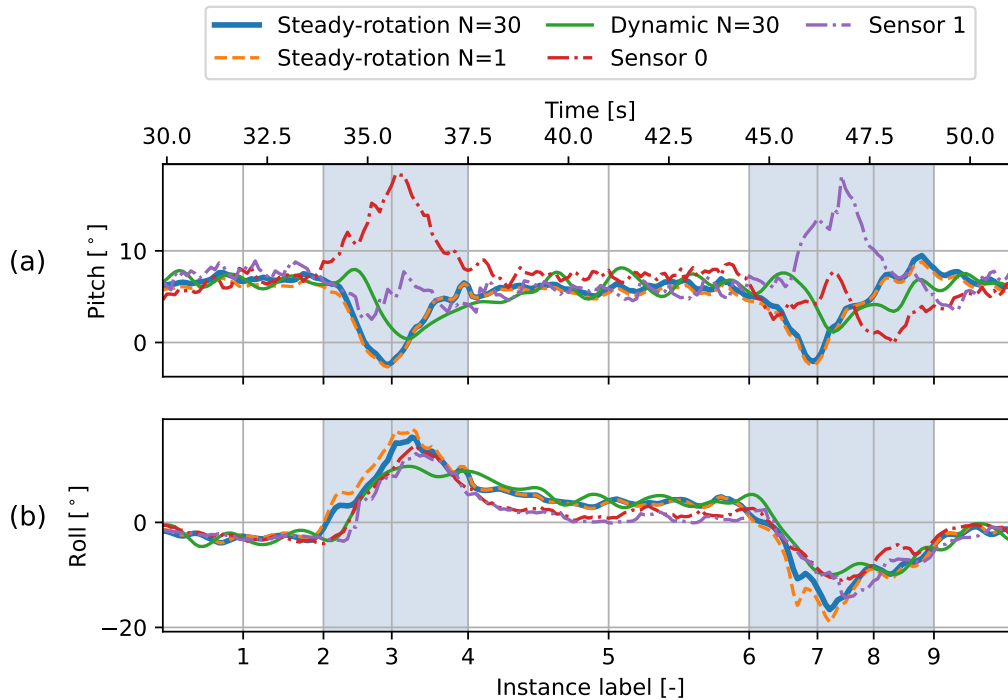
Figure 11. The pitch and roll of the kite derived from the attitude of the bridle element (with respect to the tangential plane) along the figure of eight. The results of the steady-rotation-state and dynamic analyses are depicted alongside the pitch and roll inferred from attitude measurements of the two sensors mounted to the wing, which include local effects of wing deformation. The shaded intervals indicate the turns.

4.2 Cross-check with dynamic results

The dynamic simulation requires the wing acceleration, imposing the flight path, and the tether reel-out acceleration as input. The flight trajectory is reconstructed as described in Appendix A to ensure a running simulation and ensure that the inputs are consistent with the studied figure-of-eight manoeuvre. The intensive reconstruction yields a slightly adapted tether reel-out speed with respect to the measured speed and imposes a nearly constant difference between the tether length and radial kite position in the simulation. In this paper, we refer to this difference as tether slack. The initial tether length of the simulation is chosen such that the tether slack is 0.28 m, which is the mean value observed in the steady-rotation-state results.

Figure 12 shows the tether force evolution that results from the dynamic simulation. Since the force is sensitive to the choice of the tether slack, the agreement with measurements during the straight sections confirms that the choice for the constant tether slack is reasonable. During the turns, the calculated tether force does not agree well with the measurements. The simulated force shows distinct peaks, whereas the measured force shows a more gradual increase. These differences, however, are not specific to the dynamic model but are expected to be artifacts of the wing and tether acceleration control input.
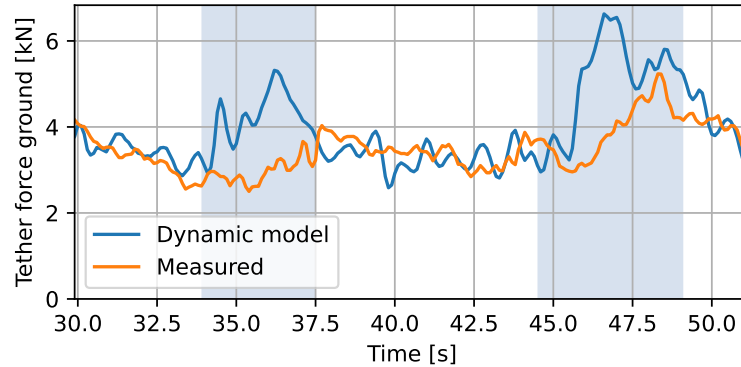
Figure 12. Tether force evolution along the figure of eight resulting from the dynamic simulation and from the flight data. The shaded intervals indicate the turns.

The resulting tether-kite lines are plotted in Fig. 10c and d. Most shapes of the reference instances show a reasonable agreement with the steady-rotation-state results. An apparent outlier is the 3rd reference instance, which occurs at the outside of the turn. This discrepancy can also be observed in Fig. 11a, in which the pitch resulting from the dynamic simulation closely follows the steady-rotation-state model results, except for the middle of the turn.

Dynamic models are in general suitable to evaluate the flight behaviour during turns as it concerns a highly dynamic manoeuvre with transient effects on the tether-kite line. These transient effects are likely to explain why in Fig. 10d the lower end of the tether of the 3rd reference instance still has a negative cross-apparent-wind displacement like its predecessor, while the corresponding steady-rotation-state result is positive over the full length. Note that the current dynamic model does not necessarily enhance accuracy by considering transient effects as it requires different assumptions, e.g., on the tether reel-out acceleration, with associated uncertainties.

4.3 Kite attitude validation

The available measurements useful for validating the motion of the tether-kite line are the wing attitude measurements. These allow for estimating the actual pitching and rolling motion of the kite and, thereby, can help with validating the models. Validating the rotational motion of the kite is particularly important for performance model development, as accurate descriptions of this motion are essential for incorporating the aerodynamics and the turning mechanism. The tether motion cannot be validated as no measurements are taken directly from the tether. Validating the tether motion is considered less important for performance model development.

Figure 11 compares the modelled pitch and roll angles of the kite element with measurements from two different sensors mounted to the wing. The same pitch and roll definitions are used to express the wing attitude measurements, provided in Appendix B. The kite attitude is inferred from these measurements by assuming that the kite is fully rigid and that the orientation of the wing relative to the bridle is defined by the depower angle α_d shown in Fig. 3. Moreover, the measurements are corrected

for misalignments with the wing reference frame. 7° is added to the measured pitch of both sensors to correct for the sensor misalignment. Similarly, 8.5° is subtracted from the roll of both sensors to correct for sensor misalignment.

Both sensors measure a similar roll along the whole figure of eight, as shown in Fig. 11. However, the pitch measured with the two sensors differs substantially during the turns. Investigating the root cause revealed a strong relationship between the difference in pitch and the steering input. Fig. 13c illustrates their relation within the 65th pumping cycle with a Pearson correlation coefficient of -0.96. A steering input causes the steering tape to pull in on one side and give slack on the other. As a result, the wing twists around the leading edge with a zero twist at the centre. The high correlation found suggests that the twist between the struts on which the sensors are mounted is measured with high precision. The pitch at the centre of the wing is assumed to be the average of the two measurements.

Figure 11 shows that the differences in pitch and roll resulting from the models and the measurements are small during the straight sections. The computed pitch and roll angles match the measurements within three degrees. Contrastingly, the two models exhibit systematic differences during the turns. In particular, the pitch exhibits larger differences during the turns. Although the dynamic result lies closer to the average measured pitch during the turns, it does not exhibit a similar peak. This discrepancy could be attributed to the high uncertainty of the position measurement during the turns, resulting in large modifications to the flight trajectory by the reconstruction. Thereby, the actual wing motion that is causing the peak in pitch might have gotten lost in the reconstruction or was not properly measured. Moreover, the steady-rotation states might not accurately capture the kite attitude during turns because they do not consider transient effects.

In general, the steady-rotation states perform reasonably well in estimating the kite attitude, both with a single tether element and 30 tether elements. This suggests that both discretisations can capture the inertial effect of the KCU during turns. The dynamic model does not necessarily produce more accurate results than the steady-rotation-state model. This can be explained by inaccuracies in the input causing errors, e.g., due to imperfections of the flight trajectory reconstruction.

4.4 Pitching Motion along a Full Pumping Cycle

To study the pitching motion of the kite outside the reel-out phase, we zoom out and evaluate multiple pumping cycles, including the 65th cycle, which contains the previously investigated figure-of-eight manoeuvre. During the reel-in phase, the kite turns less, and the associated rolling motion is small. In contrast, the pitching of the kite induced by the tether sag is more pronounced as the tether tension reduces and the weight and drag of the tether are relatively large. Both the weight and drag of the tether result in the tether sagging downwards.

Figure 14 shows the kite pitch inferred from the wing measurements and the kite pitch resulting from the steady-rotation-state analysis with 30 tether elements. The results of ten consecutive pumping cycles are depicted, starting with the 65th pumping cycle. Each cycle starts with the transition into the reel-out phase, followed by approximately four figures of eight. Subsequently, the kite is pointed towards the zenith, depowered, and reeled back in (after the last shaded interval). The cycle ends after powering up again in preparation for a new cycle.

Each cycle shows an increase in pitch after the last turn in the reel-out phase as the kite transitions into the reel-in phase. The model overestimates the pitch at the start of the reel-in and underestimates it towards the end but gives a good overall
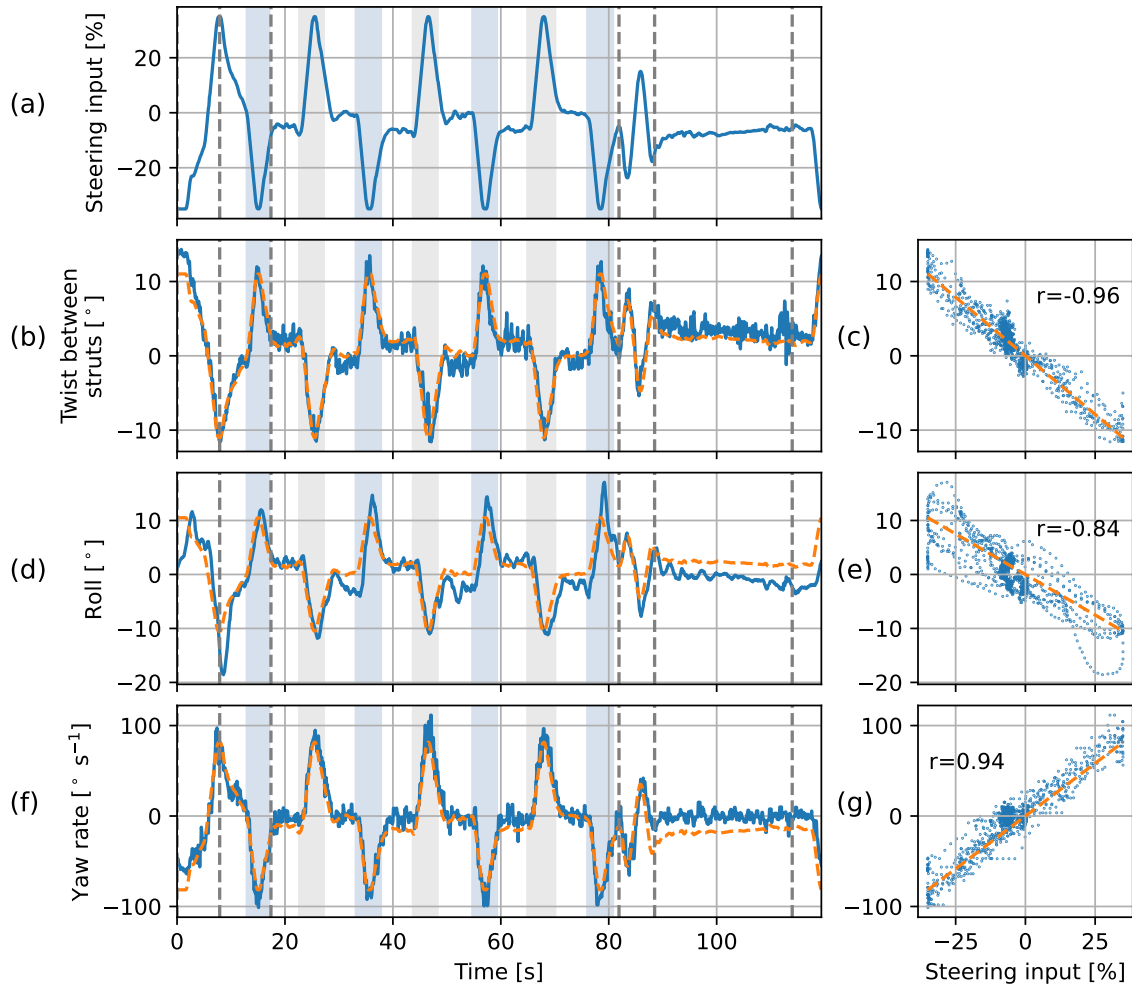
Figure 13. Relations between (**a**) the steering input and (**b, c**) the difference in pitch of the two sensors, (**d, e**) roll of the kite, and (**f, g**) yaw rate of the kite in the 65$^{\text{th}}$ pumping cycle. The orange dashed lines in the left column depict the steering input scaled with the slope found in the linear fit shown with the orange dashed lines in the right column.

agreement. There are many factors that may cause this discrepancy. One plausible explanation is that the reduced load during
400   the reel-in phase causes the kite struts, on which the sensors are mounted, to deform. The deformation is measured but not accounted for in the model and, thus, not incorporated in the computed results. Note that during the reel-in, the steering input is non-zero, as shown in Fig. 13a. This causes a pitch offset between the two sensors.
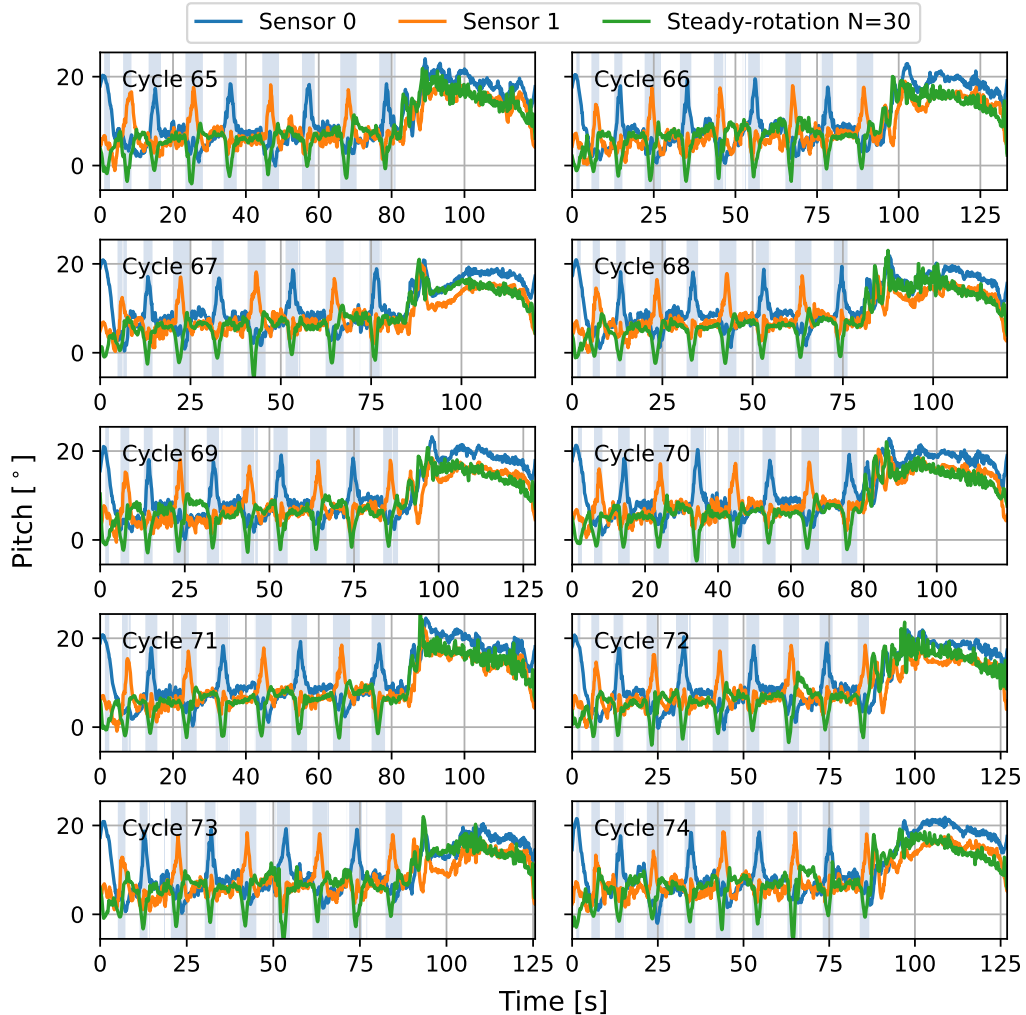
Figure 14. The pitch of the kite element with respect to the tangential plane along ten pumping cycles resulting from the steady-rotation-state analysis using 30 tether elements (T-I N=30), together with the kite pitch inferred from the wing attitude measured with two sensors. The shaded intervals indicate the turns during the reel-out phase. After the turns, the system transitions into the reel-in phase.

5 Discussion

In this section, we discuss the implications of the observed swinging motion for the performance modelling of a kite system. Different mechanisms initiate and drive a turn of a flexible kite system with a suspended control unit.

The initiation mechanism for turning flexible kites with a suspended control unit relies on twisting of the wing tips. A steering input causes the wing to twist, which increases the angle of attack at the wing tip at the inside of the turn and decreases it at the outside wing tip. This creates an aerodynamic side force component perpendicular to the kite symmetry plane and

pointing towards the turn centre. The introduction of a side component effectively rolls the resultant aerodynamic force acting on the whole kite without rolling the kite itself. In contrast to flexible kites with a suspended control unit, multi-line flexible kites that are actuated from the ground employ this mechanism to drive the whole turn; the side force is dominant in providing the centripetal force.

The driving mechanism for turning flexible kites with a suspended control unit is the rolling of the kite. As soon as the turn is initiated, the kite will roll into the turn to exert a centripetal force on the relatively heavy KCU, pulling it along. Together with the kite, the lift force generated by the top wing surface rolls into the turn and contributes to the centripetal force. The higher the mass of the KCU, the more roll is required to execute the same turn. Consequently, a smaller fraction of the lift is available to carry the weight of the airborne components and pull the tether. While the aerodynamic side force is still necessary to maintain turning, it is the roll of the kite that accommodates the largest contribution to the centripetal force and is thus considered to drive the turn.

To incorporate this turning mechanism, a single-point kite model would need the roll of the kite as an input, relying on the user to provide realistic roll angles. Another option is modelling the roll, e.g., using an empirical relationship between the roll and the steering input, as shown in Fig. 13e. However, with little extra computational cost, the roll can be resolved by modelling the kite with at least two point masses: one for the wing and one for the KCU. Thereby, it no longer needs to rely on system-specific empirical relationships for including the steering mechanism. Instead, the aerodynamic side force needed to initiate and maintain the turn can be calculated based on the deformation of the kite tips and associated aerodynamics.

Although the kite pitch does not change substantially during the reel-out phase, the tether-kite motion causes it to change substantially outside this phase. The sag-induced pitch concerns performance modelling as it affects the angle of attack experienced by the wing, which in turn affects the generated aerodynamic forces. Resolving the pitch also requires modelling the kite with at least two point masses and enables incorporating an aerodynamic model for the wing with a dependency on the angle of attack.

Complemented with an aerodynamic model of the kite, the dynamic model no longer relies on prescribing the wing acceleration. In contrast to the simulations conducted in the current analysis, simulations that solve the wing motion will be very sensitive to the wind input, which poses a large challenge to the validation of the model.

6 Conclusions

The inertia of the suspended control unit has a large effect on the roll of a flexible kite during turns in the reel-out phase. During the reel-in phase, the pitch of the kite changes due to the weight and drag of the control unit and increased tether sag. These effects are not resolved when the kite is modelled with a single point mass. With two point masses, one at the wing and one at the control unit, the steady-rotation-state model performs reasonably well in capturing the pitch and roll with little extra computational effort. Two-point models can thus be a powerful tool for the performance modelling of flexible kite systems.

The swinging motion of a kite with a suspended control unit is assessed with two approaches: approximated as a transition through steady-rotation states and solved dynamically. In contrast to the dynamic model, the steady-rotation-state model

neglects transient effects. Both approaches employ a two-point kite model extending a discretised tether model using an additional rigid element for the kite. By prescribing the cross-wind flight path of the wing, no aerodynamic model of the kite is required.

445 An alternative expression for the angular velocity underlying the steady-rotation assumption is derived that accounts for the turning of the kite. This angular velocity expression accommodates lateral accelerations on the point masses and, thereby, allows studying the lateral swinging motion of the kite. The angular velocity for turns is approximated with flight data and shows good agreement with the kite kinematics. Unlike the original angular velocity expression, the proposed expression yields a good approximation of not only the wing velocity but also of the wing acceleration.

450 The tether-kite lines resulting from the steady-rotation states show discontinuities at the junction between the tether and the kite. These indicate that the control unit has a substantial effect on the attitude of the kite and stress the need for including a separate point mass for the control unit in performance models for flexible kite systems. The steady-rotation states perform reasonably well in estimating the roll of the kite, both with a single and 30 tether elements. The computed pitch and roll angles match the measured angles within three degrees during the straight sections of the figure-of-eight manoeuvre. During 455 the turns, the peaks in the roll are overestimated and the instantaneous differences in roll may exceed five degrees, whereas the pitch exhibits more systematic differences. These systematic differences could partially be explained by the fact that the model did not account for transient effects. However, drawing a definite conclusion is challenging, as the measurements include steering-induced pitch, making the wing measurements a poor reference.

 Although the dynamic model considers transient effects, it is not more accurate in capturing the roll and pitch behavior 460 during turns than the steady-rotation states. This is expected to be primarily caused by inaccuracies in the wing acceleration and tether reel-out acceleration inputs. Due to anomalies in the flight trajectory measurements, a reconstruction was necessary to generate consistent inputs, enabling a running simulation. The reconstruction assumes that the tether slack length, defined as the difference between the tether length and radial position of the kite, remains constant. The intensity of the reconstruction adds further uncertainty to the results. Moreover, since the employed model is designed for computational efficiency, it does 465 not capture non-trivial aspects such as tether elasticity.

 Two separate mechanisms have been identified that initiate and drive a turn of a flexible kite system with a suspended control unit. A steering input causes an aerodynamic side force that initiates the turn. As soon as the turn is initiated, the kite starts to roll as it needs to pull the relatively heavy control unit into the turn. The rolled lift force provided by the top wing surface of the kite provides the largest contribution to the centripetal force and is said to drive the turn. Since a two-point kite model resolves 470 the roll, the lift force may tilt along with the kite to drive turns. Hence, it avoids intricate centripetal force modelling, as seen in a single-point kite model. Furthermore, by resolving the pitch, it allows computing the angle of attack of the wing. The angle of attack is an important input to the aerodynamic model required when solving the wing motion instead of prescribing a flight path, as done in the current study.

 The results of this study could be significantly improved with better quality flight data, more raw data, and information about 475 how measurements are conditioned and calibrated. Currently, the sensor units are mounted to the flexible wing. As a result, wing deformation and actuation of the depower angle of the wing are also measured. This could be prevented by mounting

the sensor units to the kite control unit. To find a better match between the measured and simulated tether forces, it would be interesting to incorporate variable tether slack and account for stretching in the dynamic simulation. A stepping stone could be to wrap the simulation in an optimisation problem to find the tether acceleration input that produces the measured tether force and cross-check the results with the tether lengths resulting from the steady states. More accurate tether length information in the experimental data would greatly help such analysis. Moreover, the flight trajectory reconstruction could be enhanced with this information, as well as with more advanced state estimation techniques. Finally, both the stead-rotation-state and dynamic models could still benefit from refining the wind modelling and fine-tuning the model parameters.

Data availability. The complete test flight data, including 87 pumping cycles spanning a total flight time of 265 minutes, are available in open access from (Schelbergen et al., 2023). The specific pumping cycle underlying this study and the Python code for the data analysis are available in open source from (Schelbergen).

Appendix A: Flight Trajectory Reconstruction

The kinematics of the wing recorded in the flight data show inconsistencies in the measured tether reel-out speed and are reconstructed in a preprocessing step to remove anomalies. The dynamic simulation relies on the recorded wing kinematics and tether reel-out speed for its input. Directly using these recorded quantities as input leads to faulty simulations, and a workaround is needed to obtain coherent input. The reconstruction is carried out for the full 65$^{\text{th}}$ pumping cycle.

A preliminary evaluation of the wing kinematics in the flight data shows that the vertical speed does not fully agree with the derivative of the vertical position of the wing, even though it does for the horizontal components. The largest mismatch occurs during the turns, where the recorded vertical speed is more negative than the derivative of the vertical position. The recorded vertical position is GPS data enhanced with barometer measurements. However, we expect that the vertical speed is not updated accordingly.

The inconsistent vertical speed leads to a discrepancy between the derivative of the measured radial position $\hat{r}_{\text{k}}$ and the measured radial component of the wing velocity $\hat{v}_{\text{k,r}}$, while in theory, they should be the same. These quantities are depicted with the blue and red lines, respectively, in Fig. A1c. The radial component of the wing velocity is calculated with:

$$v_{\text{k,r}} = \frac{\mathbf{r}_{\text{k}} \cdot \mathbf{v}_{\text{k}}}{\|\mathbf{r}_{\text{k}}\|},\tag{A1}$$

in which $\mathbf{r}_{\text{k}}$ and $\mathbf{v}_{\text{k}}$ are the position and velocity of the wing, respectively. An objective of the intended flight trajectory reconstruction is to ensure that the updated radial component of the wing velocity and the derivative of the radial position agree.

As an additional check, the derivative of the measured radial position of the wing $\hat{r}_{\text{k}}$ is compared to the measured tether reel-out speed $\hat{\dot{l}}_{\text{t}}$ (dotted black line in Fig. A1c). The derivative of the radial position shows large fluctuations around the tether reel-out speed in the reel-out phase. The magnitude of the fluctuations conflicts with our expectation that the changes in tether

slack (difference between the tether length and radial position of the kite) and stretch are small in this phase. Towards the end of the right turns (at the end of the blue intervals), the derivative of the radial position even tends to become shortly negative.
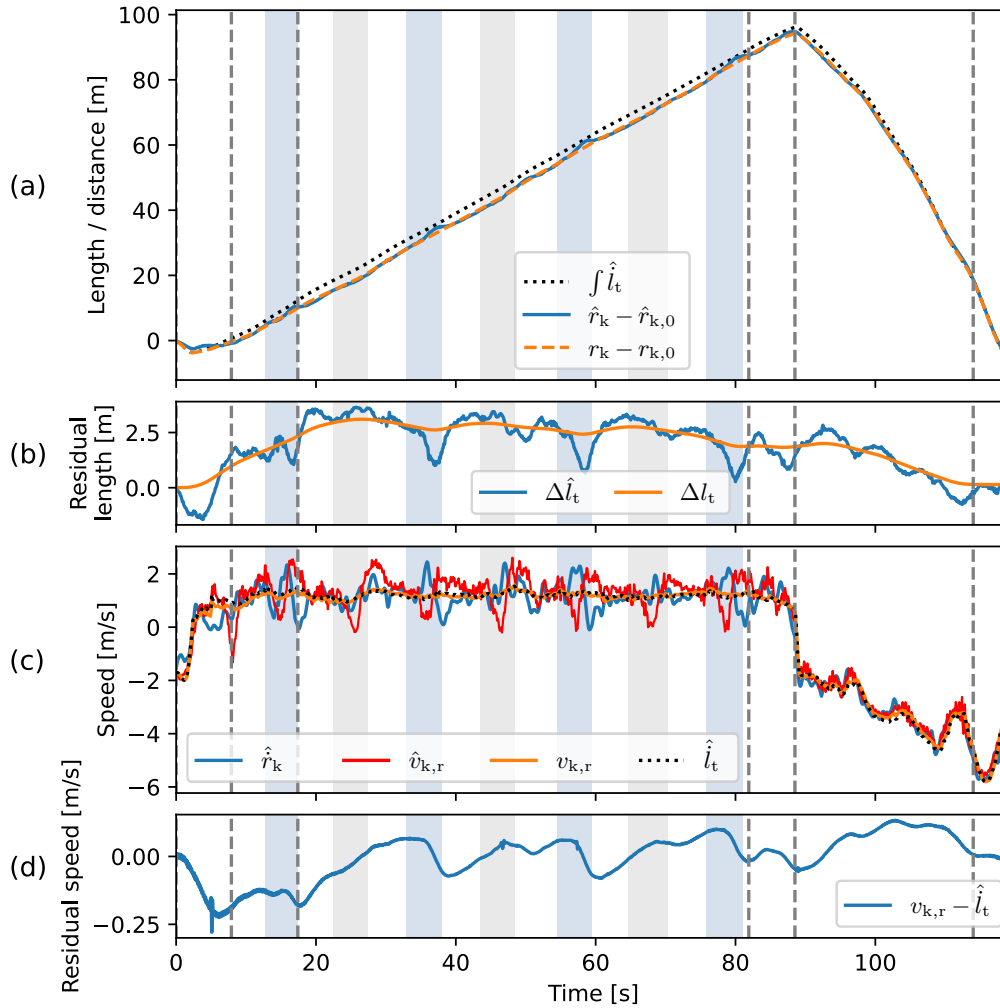
Figure A1. (a) Evolution of unstrained tether length $\int \hat{l}_t$ and the measured and reconstructed radial distances of the wing, $\hat{r}_k$ and r_k, all with their initial values subtracted. (b) Difference between the tether length and the measured radial distance of the wing $\Delta \hat{l}_t$ and its equivalent after the reconstruction Δl_t. (c) Time-derivative of measured radial position of the wing $\dot{\hat{r}}_k$, measured and reconstructed radial speeds of the wing, $\hat{v}_{k,r}$ and $v_{k,r}$, and measured tether reel-out speed $\dot{\hat{l}}_t$. (d) Residual between the tether reel-out speed and reconstructed radial speed. The intervals shaded grey and blue indicate left and right turns, respectively, from a downwind perspective.

Figure A1a shows how the integrated measured reel-out speed (dotted black line) evolves with respect to the measured radial position of the wing $\hat{r}_k$ (blue line). During the right turns, the inferred tether length increases approximately linearly, while the radial position exhibits subtle local maxima. These local maxima coincide with the large discrepancies between the derivative

510

of the radial position and the tether reel-out speed observed in Fig. A1c. Note that the tether length lines depict the relative lengths with respect to the start of the pumping cycle. The lines need to be shifted up with their initial values to obtain their respective absolute values. Unfortunately, we do not know the absolute tether length as it is not measured directly.

515   The residual between the inferred tether length and measured radial position $\Delta \hat{l}_t$ is shown in Fig. A1b. During the right turns, the residual changes roughly 2 m (depth of the valley) within a couple of seconds. The corresponding relatively large increase in radial position can partly be attributed to a decrease in tether slack and an increase in tether stretch. However, the magnitude of the change is deemed to be too large to be attributed only to changes in these quantities. Note that also here, the line may shift vertically depending on the initial values. As such, we can not draw conclusions based on the magnitude of the

520   residual but merely on how it changes with time. The given residual length has an unknown offset with respect to the tether slack. Note that the tether slack cannot be negative.

The maxima in the recorded radial position do not need to be purely physical. Another possible cause is GPS inaccuracy during manoeuvres, which has previously been reported in the literature. Borobia et al. (2018) reported measured radial position exceeding varying more than 3 m while none was expected. Considering the imprecision of the recorded position, we opt to

525   adapt the wing kinematics by letting the radial wing speed follow the measured reel-out speed as closely as possible.

The flight trajectory reconstruction is obtained using a discrete-time optimisation problem that minimises the error between the modelled radial wing speed and recorded tether reel-out speed while limiting the bias between the modelled and recorded wing position

$$
\min_{\mathbf{r}_k(\cdot), \mathbf{v}_k(\cdot), \mathbf{a}_k(\cdot)} \quad \sum_{i=0}^{N} \left[\mathrm{w} \left(v_{k,r} - \hat{\dot{l}}_t \right)^2 + (\mathbf{r}_k - \hat{\mathbf{r}}_k)^\top (\mathbf{r}_k - \hat{\mathbf{r}}_k) \right]_{t=\frac{i}{10}}
\tag{A2}
$$

$$
\text{s.t.} \quad \mathbf{a}_k = \dot{\mathbf{v}}_k = \ddot{\mathbf{r}}_k .
$$

530   Quantities marked with a hat indicate measured quantities, whereas the absence of a hat indicates modelled quantities. A discrete function is used for the acceleration of the wing, and continuous trajectories are used for the velocity and position of the wing. The decision variables consist of the wing accelerations during the control intervals $\mathbf{a}_k(\cdot)$ and the velocities $\mathbf{v}_k(\cdot)$ and positions $\mathbf{r}_k(\cdot)$ at the control interval boundaries. N is the number of time steps, and the weighing factor $\mathrm{w} = 25$ is chosen as it leads to a good balance between the two objectives. Note that having matching reel-out and radial wing speeds does not

535   necessarily mean that also the tether length is the same as the radial position. However, it does mean that the tether slack stays constant.

In line with the dynamic simulation, the fitting problem uses discrete control input trajectories. It assumes a constant acceleration within each simulation time step of 0.1 s. Between the corresponding control intervals, the values may vary. Due to the step function form of the acceleration, the velocity and position are linear and quadratic functions, respectively, within the

540   control intervals. These low-order forms allow for sufficient detail due to the small time step. The fitting problem is solved in CasADi using a multiple-shooting approach. This approach is not hindered by integration drift causing an accumulating error with time.

The flight trajectory reconstruction results are shown with the orange lines in Fig. A1. The reconstruction shaves off the local maxima in the recorded radial position as can be observed in Fig. A1a. Figure A1c shows that the reconstructed radial

545   wing speed follows the measured reel-out speed more closely. The residual speed, which is penalised by the first term of the objective function, is illustrated in Fig. A1d. The optimiser reduces the position bias, which is penalised by the second term of the objective function, by allowing small changes to the radial wing speed with respect to the measured reel-out speed. As a consequence, the reconstruction does not lower the residual length substantially but keeps it close to the original residual length, as can be seen in Fig. A1b.

550   We use the reconstructed radial wing acceleration $a_{k,r}$ as tether reel-out acceleration input $\ddot{l}_t$ for the simulation. Thus, we do not only reconstruct the flight trajectory but also modify the tether reel-out speed with respect to the measurements. As a result, the tether slack remains constant in the simulation and is set by the choice for the initial tether length. In reality, changes in slack length will occur, especially during the transition phases. Therefore, this approach might be sub-optimal for simulating the entire pumping cycle. Nonetheless, it is suitable for simulating intervals where only small tether slack and stretch changes

555 are expected, such as the reel-out phase.

     We acknowledge that the flight trajectory reconstruction might not be strictly valid. Nevertheless, it serves the higher aim of this study and allows simulating a short interval encompassing a figure of eight during reel-out. A more educated reconstruction would require a lot more resources and probably more testing and is recommended as a possible future improvement.

Appendix B: Pitch and Roll Angle Definitions

560 Expressing the attitude of the kite using pitch and roll angles with respect to the wind reference frame gives large variations of these angles along the flight trajectory. Consequently, the kite attitude is difficult to interpret from these angles. Variations are smaller when the pitch and roll angles are expressed with respect to the tangential plane, which is perpendicular to the position vector of the kite and shown with the black rectangle in Fig. B1. The variations are smaller since the up-direction (positive z-axis) of the kite and the direction of the position vector in the wind reference frame are not far apart, especially during the

565 reel-out phase, where the tether is relatively straight due to the high pulling force of the kite.

B1   Measured attitude of the kite

The rotation matrix for the transformation from the earth to the tangential reference frame is calculated by:

$$\mathbb{T}_{\tau e} = \begin{bmatrix} \sin\hat{\beta} & 0 & -\cos\hat{\beta} \\ 0 & 1 & 0 \\ \cos\hat{\beta} & 0 & \sin\hat{\beta} \end{bmatrix} \begin{bmatrix} \cos(\hat{\varphi}+\hat{\varphi}_{we}) & \sin(\hat{\varphi}+\hat{\varphi}_{we}) & 0 \\ -\sin(\hat{\varphi}+\hat{\varphi}_{we}) & \cos(\hat{\varphi}+\hat{\varphi}_{we}) & 0 \\ 0 & 0 & 1 \end{bmatrix}, \tag{B1}$$

in which subscripts τ, w, and e refer to the tangential, wind, and earth reference frames, respectively, the hat denotes a measured

570 quantity, β is the elevation angle, and φ is the azimuth angle.
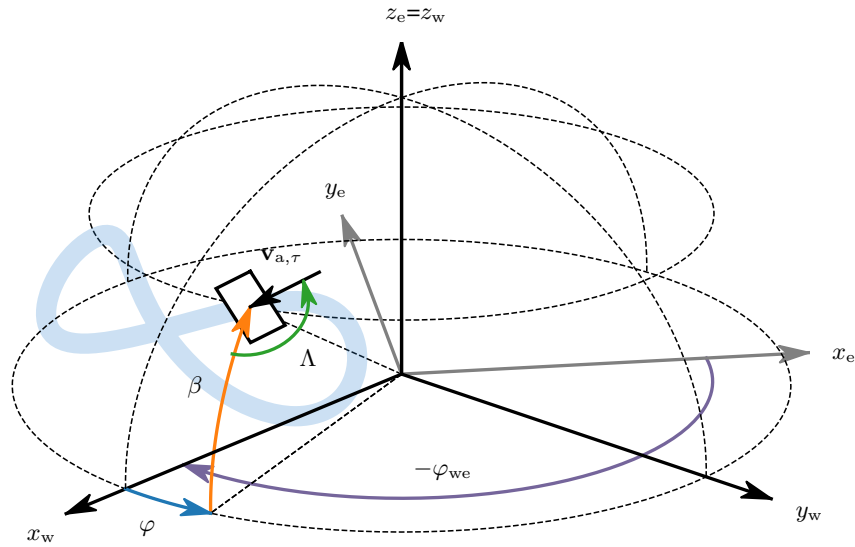
Figure B1. Earth reference frame x_e, y_e, z_e and wind reference frame x_w, y_w, z_w together with the yawed tangential plane lying on the projection of a figure-of-eight flight path. This plane is yawed such that it heads into the apparent wind velocity and serves as a departure point for expressing the kite attitude, illustrated in Fig. B2. The corresponding yaw angle Λ is equal to the kite heading in case of zero side slip.

The measured pitch, roll, and yaw of the wing of the kite are expressed using 3-2-1 Euler angles. The corresponding rotation matrix for the transformation from the earth to the top wing surface reference frame is calculated by:

$$\mathbb{T}_{\text{tws-e}} = \begin{bmatrix} 1 & 0 & 0 \\ 0 & \cos\hat{\phi} & \sin\hat{\phi} \\ 0 & -\sin\hat{\phi} & \cos\hat{\phi} \end{bmatrix} \begin{bmatrix} \cos\hat{\theta} & 0 & -\sin\hat{\theta} \\ 0 & 1 & 0 \\ \sin\hat{\theta} & 0 & \cos\hat{\theta} \end{bmatrix} \begin{bmatrix} \cos\hat{\psi} & \sin\hat{\psi} & 0 \\ -\sin\hat{\psi} & \cos\hat{\psi} & 0 \\ 0 & 0 & 1 \end{bmatrix}, \tag{B2}$$

in which subscripts tws and e refer to the top wing surface and earth reference frames, respectively, ϕ is the roll angle, θ is the
575 pitch angle, and ψ is the yaw angle.

The attitude of the kite is not affected by the depower signal and can be approximated by pitching the wing reference frame with the negative of the depower angle α_d depicted in Fig. 3

$$\mathbb{T}_{\text{b-tws}} = \begin{bmatrix} \cos\alpha_d & 0 & \sin\alpha_d \\ 0 & 1 & 0 \\ -\sin\alpha_d & 0 & \cos\alpha_d \end{bmatrix}, \tag{B3}$$

in which subscript b denotes the bridle reference frame. The depower angle is calculated using a geometrical model from the
580 power setting (Schelbergen and Schmehl, 2020) and yields a nose-down pitch angle of roughly 6.6° during the reel-in phase.

The rotation matrix for the transformation from the tangential to the bridle reference frame is derived from the previously presented matrices:

$$\mathbb{T}_{\text{b}\tau} = \mathbb{T}_{\text{b-tws}} \mathbb{T}_{\text{tws-e}} \mathbb{T}_{\tau\text{e}}^{\top}. \tag{B4}$$

A rotation matrix can be represented with a set of 3-2-1 Euler angles. The yaw, pitch, and roll corresponding to these three angles can be calculated using the lower expressions:

$$\psi = \arctan2\left(\mathbb{T}_{12}, \mathbb{T}_{11}\right), \tag{B5}$$

$$\theta = -\arctan2\left(\mathbb{T}_{13}, \sqrt{\mathbb{T}_{23}^2 + \mathbb{T}_{33}^2}\right), \tag{B6}$$

$$\phi = \arctan2\left(\mathbb{T}_{23}, \mathbb{T}_{33}\right), \tag{B7}$$

in which $\mathbb{T}_{ij}$ denotes the transformation matrix element at the ith row and j^{th} column. The Euler angles corresponding to $\mathbb{T}_{b\tau}$ are denoted without a subscript. The definitions of the pitch and roll angles are illustrated in Fig. B2, taking the yawed tangential plane as the point of departure.
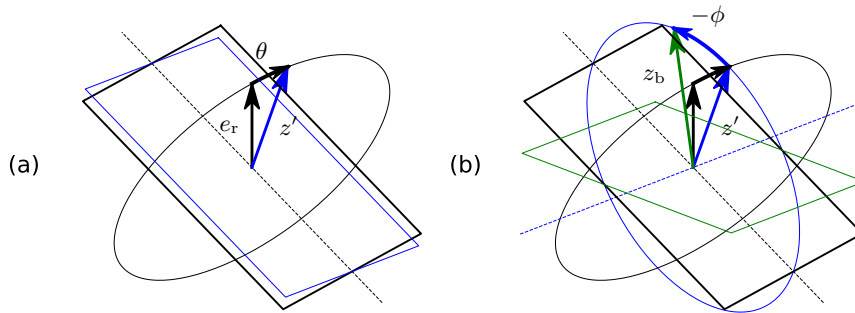
Figure B2. Last two rotations in the 3-2-1 sequence (Euler angles) to get from the tangential to the bridle reference frame: (**a**) a positive pitch rotation and (**b**) a negative roll rotation. The black rectangle illustrates the yawed tangential plane, introduced in Fig. B1.

Λ in Fig. B1 describes the orientation of the tangential projection of the modelled apparent wind velocity, also shown in Fig. 5. In case of no side slip, Λ equals the heading angle. The heading angle inferred from measurements and Λ has a small periodic misalignment (not plotted), which may indicate a side slip. However, the constant wind assumption and measurement errors introduce too much uncertainty to confirm this. Also, the side slip angle was not measured in the studied test flight and thus can not be validated. Nevertheless, some side slip can be expected, as previously shown in the experiments by Oehler and Schmehl (2019).

B2 Modelled attitude of the kite

Expressing the Euler angles of the kite element of the model requires assigning a local reference frame to the element. The model does not specify a full reference frame but only specifies the axial direction of the element. This axial direction is used as the z-axis for the local reference frame. To differentiate between the roll and pitch, also the x-axis and y-axis need to be specified. The x-axis is chosen such that it lies in the plane spanned by the position vector and the vertical direction z_e. The y-axis then follows from the other two axes and is oriented horizontally.

Other than for securing the alignment between the roll and pitch definitions of the measured and modelled kite attitude, the yaw of the tether is not of interest to this study. It does not affect the kite attitude itself and, therefore, the resulting yaw angles are left out of Fig. 11. The modelled yaw of the kite is similar to that inferred from the wing attitude measurements and, thereby, facilitates comparing the measured and modelled roll and pitch.

Author contributions. Conceptualisation, M.S. and R.S.; methodology, M.S.; software, M.S.; investigation, M.S.; writing—original draft preparation, M.S.; writing—review and editing, R.S.; supervision, R.S.; funding acquisition, R.S. All authors have read and agreed to the published version of the manuscript.

Competing interests. Roland Schmehl is a member of the editorial board of Wind Energy Science. He is also a co-founder of and advisor for the start-up company Kitepower B.V., which is commercially developing a 100 kW kite power system and provided their test facilities and staff for performing the in situ measurements described in this article. Both authors were financially supported by the European Union's Horizon 2020 project REACH, which also provided funding for Kitepower B.V.

Acknowledgements. This research was part of the project REACH (H2020-FTIPilot-691173), funded by the European Union's Horizon 2020 research and innovation programme under grant agreement No. 691173, and the project AWESCO (H2020-ITN-642682) funded by the European Union's Horizon 2020 research and innovation programme under the Marie Skłodowska-Curie grant agreement No. 642682. The authors are grateful to Kitepower B.V. for making the flight data available in open access and for sharing expertise about the system, in particular Joep Breuer for asking critical questions. Also, we would like to thank Arthur Roullier on whose MSc thesis this work builds upon and Jochem de Schutter for his tips on implementing the dynamic simulation.

References

Andersson, J. A. E., Gillis, J., Horn, G., Rawlings, J. B., and Diehl, M.: CasADi – A software framework for nonlinear optimization and optimal control, Mathematical Programming Computation, 11, 1–36, https://doi.org/10.1007/s12532-018-0139-4, 2019.

Borobia, R., Sanchez-Arriaga, G., Serino, A., and Schmehl, R.: Flight-Path Reconstruction and Flight Test of Four-Line Power Kites, Journal of Guidance, Control, and Dynamics, 41, 2604–2614, https://doi.org/10.2514/1.G003581, 2018.

Bosch, A., Schmehl, R., Tiso, P., and Rixen, D.: Nonlinear Aeroelasticity, Flight Dynamics and Control of a Flexible Membrane Traction Kite, in: Airborne Wind Energy, edited by Ahrens, U., Diehl, M., and Schmehl, R., Green Energy and Technology, chap. 17, pp. 307–323, Springer, Berlin Heidelberg, https://doi.org/10.1007/978-3-642-39965-7_17, 2013.

Breukels, J., Schmehl, R., and Ockels, W.: Aeroelastic Simulation of Flexible Membrane Wings based on Multibody System Dynamics, in: Airborne Wind Energy, edited by Ahrens, U., Diehl, M., and Schmehl, R., Green Energy and Technology, chap. 16, pp. 287–305, Springer, Berlin Heidelberg, https://doi.org/10.1007/978-3-642-39965-7_16, 2013.

Cayon, O.: Fast aeroelastic model of a leading-edge inflatable kite for the design phase of airborne wind energy systems, Master's thesis, Delft University of Technology, http://resolver.tudelft.nl/uuid:aede2a25-4776-473a-8a75-fb6b17b1a690, 2022.

Duport, C.: Modeling with consideration of the fluid-structure interaction of the behavior under load of a kite for auxiliary traction of ships, Phd thesis, ENSTA Bretagne, https://tel.archives-ouvertes.fr/tel-02383312, 2018.

Fagiano, L., Quack, M., Bauer, F., Carnel, L., and Oland, E.: Autonomous Airborne Wind Energy Systems: Accomplishments and Challenges, Annual Review of Control, Robotics, and Autonomous Systems, 5, https://doi.org/10.1146/annurev-control-042820-124658, 2022.

Fechner, U., van der Vlugt, R., Schreuder, E., and Schmehl, R.: Dynamic Model of a Pumping Kite Power System, Renewable Energy, 83, 705–716, https://doi.org/10.1016/j.renene.2015.04.028, 2015.

Folkersma, M. A. M.: Aeroelasticity of Membrane Kites: Airborne Wind Energy Applications, Ph.D. thesis, Delft University of Technology, Delft, https://doi.org/10.4233/uuid:eae39f5a-49bc-438b-948f-b6ab51208068, 2022.

Geschiere, N.: Dynamic modelling of a flexible kite for power generation, Master's thesis, Delft University of Technology, http://resolver.tudelft.nl/uuid:6478003a-3c77-40ce-862e-24579dcd1eab, 2014.

Gohl, F. and Luchsinger, R. H.: Simulation based wing design for kite power, in: Airborne Wind Energy, edited by Ahrens, U., Diehl, M., and Schmehl, R., Green Energy and Technology, chap. 18, pp. 325–338, Springer, Berlin Heidelberg, https://doi.org/10.1007/978-3-642-39965-7_18, 2013.

Kitepower B.V.: Onshore Containerised AWES-100 Kitepower Falcon, https://thekitepower.com/product/.

Loyd, M. L.: Crosswind kite power, Journal of Energy, 4, 106–111, https://doi.org/10.2514/3.48021, 1980.

Oehler, J. and Schmehl, R.: Aerodynamic characterization of a soft kite by in situ flow measurement, Wind Energ. Sci., 4, 1–21, https://doi.org/10.5194/wes-4-1-2019, 2019.

Oehler, J., van Reijen, M., and Schmehl, R.: Experimental Investigation of Soft Kite Performance During Turning Maneuvers, Journal of Physics: Conference Series, 1037, 052 004, https://doi.org/10.1088/1742-6596/1037/5/052004, 2018.

Peschel, J., Breuer, J., and Schmehl, R.: Kitepower – Commercializing a 100 kW Mobile Wind Energy System, in: Book of Abstracts of the International Airborne Wind Energy Conference (AWEC 2017), edited by Diehl, M., Leuthold, R., and Schmehl, R., pp. 47–51, University of Freiburg | Delft University of Technology, Freiburg, Germany, http://resolver.tudelft.nl/uuid:9e9a6bdb-f5f4-4868-bed6-f25dc5ee42f0, 2017.

Poland, J.: Modelling aeroelastic deformation of soft wing membrane kites, Master's thesis, Delft University of Technology, http://resolver. tudelft.nl/uuid:39d67249-53c9-47b4-84c0-ddac948413a5, 2022.

Rapp, S., Schmehl, R., Oland, E., and Haas, T.: Cascaded Pumping Cycle Control for Rigid Wing Airborne Wind Energy Systems, Journal
660   of Guidance, Control, and Dynamics, 42, 2456–2473, https://doi.org/10.2514/1.G004246, 2019.

Roullier, A.: Experimental analysis of a kite system's dynamics, Master's thesis, EPFL, https://doi.org/10.5281/zenodo.7752407, 2020.

Salma, V., Friedl, F., and Schmehl, R.: Reliability and Safety of Airborne Wind Energy Systems, Wind Energy, 23, 340–356, https://doi.org/10.1002/we.2433, 2019.

Schelbergen, M.: Swinging Motion of a Kite, https://github.com/awegroup/swinging-kite.

665 Schelbergen, M. and Schmehl, R.: Validation of the quasi-steady performance model for pumping airborne wind energy systems, Journal of Physics Conference Series, 1618, 032 003, https://doi.org/10.1088/1742-6596/1618/3/032003, 2020.

Schelbergen, M., Schmehl, R., Buchholz, B., Breuer, J., and Peschel, J.: Kitepower flight data acquired on 8 October 2019, Dataset, 4TU.Centre for Research Data, https://doi.org/10.4121/19376174, 2023.

Schmehl, R. and Oehler, J.: 25 m^2 LEI V3 tube kite transitioning to traction phase and starting to fly figure eight manoeuvres. Video footage
670   of onboard camera, TIB AV Portal, Copernicus Publications, https://doi.org/10.5446/37583, 2018.

Sánchez-Arriaga, G., Pastor-Rodríguez, A., Sanjurjo-Rivo, M., and Schmehl, R.: A lagrangian flight simulator for airborne wind energy systems, Applied Mathematical Modelling, 69, 665–684, https://doi.org/10.1016/j.apm.2018.12.016, 2019.

Thedens, P.: An Integrated Aero-Structural Model for Ram-Air Kite Simulations With Application to Airborne Wind Energy, Ph.D. thesis, Delft University of Technology, Delft, https://doi.org/10.4233/uuid:16e90401-62fc-4bc3-bf04-7a8c7bb0e2ee, 2022.

675 Vermillion, C., Cobb, M., Fagiano, L., Leuthold, R., Diehl, M., Smith, R. S., Wood, T. A., Rapp, S., Schmehl, R., Olinger, D., and Demetriou, M.: Electricity in the Air: Insights From Two Decades of Advanced Control Research and Experimental Flight Testing of Airborne Wind Energy Systems, Annual Reviews in Control, 52, 330–357, https://doi.org/10.1016/j.arcontrol.2021.03.002, 2021.

Williams, P.: Cable Modeling Approximations for Rapid Simulation, Journal of Guidance, Control, and Dynamics, 40, 1779–1788, https://doi.org/10.2514/1.G002354, 2017.

680 Williams, P., Lansdorp, B., and Ockels, W. J.: Modeling and Control of a Kite on a Variable Length Flexible Inelastic Tether, in: Proceedings of the AIAA Modeling and Simulation Technologies Conference and Exhibit, Hilton Head, SC, USA, https://doi.org/10.2514/6.2007-6705, 2007.

Zanon, M., Gros, S., Andersson, J., and Diehl, M.: Airborne Wind Energy Based on Dual Airfoils, IEEE Transactions on Control Systems Technology, 21, 1215–1222, https://doi.org/10.1109/TCST.2013.2257781, 2013.